

Analytical renormalization group approach to competing orders at charge neutrality in twisted bilayer graphene

Eric Brillaux, David Carpentier , Andrei A. Fedorenko , and Lucile Savary 

Univ Lyon, ENS de Lyon, Univ Claude Bernard, CNRS, Laboratoire de Physique, F-69342 Lyon, France

 (Received 16 December 2020; revised 30 May 2022; accepted 19 July 2022; published 30 August 2022)

We investigate twisted bilayer graphene near charge neutrality using a generalized Bistritzer-MacDonald continuum model accounting for corrugation effects. The Fermi velocity vanishes for particular twist angles properly reproducing the physics of the celebrated magic angles. Using group representation theory, we identify all contact interaction potentials compatible with the symmetries of the model. This enables us to identify two classes of quartic interactions leading to either the opening of a gap or to nematic ordering. We then implement a renormalization group analysis to study the effect of quantum fluctuations on the appearance of these states for twist angles approaching the first magic value. This combined group theory-renormalization study reveals that the proximity to the first magic angle favors the occurrence of a layer-polarized, gapped state with a spatial modulation of interlayer correlations, which we call a nematic insulator.

DOI: [10.1103/PhysRevResearch.4.033168](https://doi.org/10.1103/PhysRevResearch.4.033168)

I. INTRODUCTION

Fascinating states of matter arise when interactions overcome the kinetic energy of their constituents. In normal metals, the screening of the Coulomb interaction renormalizes its strength downwards in a dramatic way. But when the energy of electrons depends very little on the momentum, i.e., when the energy bandwidth vanishes, even weak interactions become dominant. The latter lead to exotic states, radically different from those occurring as instabilities of conventional metals. The prominent example of such systems is provided by Landau levels in which the strong magnetic field quenches the kinetic energy, and where in turn interactions give rise to the fractional quantum Hall effects [1,2]. More recently, a different class of materials with a vanishing bandwidth was uncovered in twisted bilayer graphene (TBG). When two sheets of graphene are rotated with respect to one another by a small angle of about 1.1° , a large moiré pattern forms with several thousands of atoms per unit cell. Remarkably, for some twist angles—the so-called magic angles—the electrons' Fermi velocity vanishes exactly [3]. Moreover, the corresponding energy bandwidth is minimal, and the “active bands” are well separated from excited bands [3–6].

The prospect of the appearance of exotic correlated phases led to a tremendous experimental effort, resulting in the discovery of correlated insulators, possibly-unconventional superconductivity [7–10], ferromagnetic states and anomalous Hall effect in TBG, but also in thicker van der Waals

heterostructures such as trilayer graphene [11–14]. The tunability of TBG by electronic gating was crucial to unveil this remarkably rich phase diagram. While the origin of the superconductivity remains unclear [15–22], evidence is mounting toward the strongest insulator emerging near the first magic angle at charge neutrality—where band theory alone would predict a semimetal—with a charge gap of around 0.86 meV in the most angle-homogeneous devices [23]. Scanning measurements detect a three-fold rotation symmetry breaking by this state [22,24,25]. The aim of this article is to unveil the nature of this correlated insulator present in TBG at charge neutrality when the energy bandwidth vanishes close to the first magic angle.

The study of interacting phases in systems with vanishing bandwidth is however notoriously difficult and to achieve the aforementioned goal, we develop methodology to analyze the competition between different types of interactions in systems where the characteristic kinetic energy vanishes. Our strategy is based on the combination of an algebraic identification of interactions that preserve the symmetries of the low-energy description and a renormalization group (RG) approach to incorporate the effects of quantum fluctuations on the prevalence of these competing states. Such an RG procedure treats all interactions on an equal footing, irrespective of their relative amplitudes and incorporates the effects of quantum fluctuations beyond mean-field and perturbative approximations. In the case of TBG, an additional obstacle arises: the absence of a simple description of the moiré pattern. We resort to a description of this moiré as a (noninteracting) continuum model of two twisted layers of graphene coupled nonperturbatively by several types of interlayer hoppings. The main outcome of these interlayer hoppings is to decrease the energy bandwidth and renormalize the associated Fermi velocity, leading to its vanishing at the magic twist angles.

We then make two simplifying assumptions. The first is that we consider only contact (short-ranged) interactions.

Published by the American Physical Society under the terms of the [Creative Commons Attribution 4.0 International](https://creativecommons.org/licenses/by/4.0/) license. Further distribution of this work must maintain attribution to the author(s) and the published article's title, journal citation, and DOI.

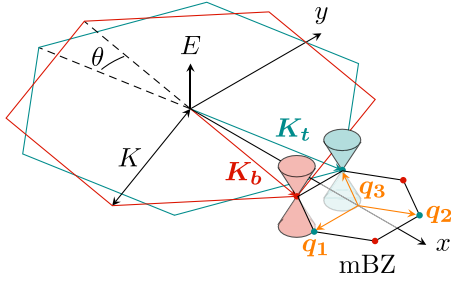


FIG. 1. In a continuum model, the relative twist of the top (green) and bottom (red) layers by an angle θ leads to one mini-Brillouin zone (mBZ) for each valley of monolayer graphene. The two Dirac cones of the same valley, \mathbf{K}_t and \mathbf{K}_b , set the sides the mBZ of size $2K \sin(\theta/2)$, where $K = |\mathbf{K}_{t,b}|$ is the Dirac momentum of monolayer graphene. Electron hoppings between the two layers involve a small momentum transfer \mathbf{q}_j , $j = 1, 2, 3$ between \mathbf{K}_t and each of the three nearest \mathbf{K}_b nodes of the mBZ.

The second is that we focus on a model where the valleys are treated independently, i.e., we consider interactions within a single valley. This latter assumption can be viewed in the context of TBG—where recent theoretical work suggests the interacting ground state is valley polarized—as a mean-field treatment of valley polarization, assuming it is the strongest stabilization mechanism, and working from there.

By formal group theory considerations, we then identify all symmetry-related (short-ranged) interactions and develop a renormalization group (RG) scheme to study their scale dependent couplings. The vanishing of the bandwidth when approaching the magic angle manifests through a singular behavior of the RG: indeed, any interacting potential, while usually treated within perturbation theory, now corresponds to a dominant energy scale. To overcome this difficulty, we monitor the scaling behavior of all interacting potentials when approaching the first magic angle. It is noteworthy that our approach becomes *more controlled* near the magic angle: there, the Fermi velocity vanishes and the relative anomalous corrections scale like $1/(\epsilon v)$ where ϵ is the small RG control parameter. We find that, as the twist angle approaches the first magic value, a state with both a gap opening and a periodic modulation of interlayer correlations is favored. We call this phase a *nematic insulator*.

II. FREE ELECTRON MODEL

Following the seminal work of Ref. [26], we treat TBG as a periodic moiré superlattice characterized by a twist angle θ . The top and bottom Dirac cones of the same valley, denoted \mathbf{K}_t and \mathbf{K}_b , delineate the mini-Brillouin zone (mBZ) of the superlattice (Fig. 1). Focusing on the low energy and long wavelength description of TBG, we restrict ourselves to small momentum transfers that are diagonal in valley, and thus occur within a single mBZ [27]. The characteristic kinetic energy scale of the model, set by the typical difference of kinetic energy of electrons in different layers, is $E_c = 2v_0K \sin(\theta/2)$, where v_0 and K are respectively the Fermi velocity and the Dirac momentum of monolayer graphene. In addition to the kinetic energy in each layer, the single-particle Hamiltonian

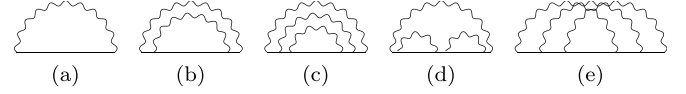


FIG. 2. Diagrammatic expansion of the electron self-energy to order 6 in the interlayer hopping amplitude $\alpha = w_1/E_c$ relative to the kinetic energy E_c . The wavy line represents a pair of opposite hopping processes, summed over all channels with a transfer of momentum $\pm\mathbf{q}_j$, $j = 1, 2, 3$. Diagram (a) is of order α^2 , diagram (b) of order α^4 , and diagrams [(c)–(e)] are of order α^6 . The expansion is nonperturbative in the relative strength β between hoppings off-diagonal and diagonal in sublattices.

involves two different interlayer hopping amplitudes. First, the amplitude w_1 of interlayer hopping that is off-diagonal in graphene sublattice is typically of order $w_1 \approx 110$ meV [26,28]. Its strength relative to the kinetic energy is measured by the dimensionless parameter $\alpha = w_1/E_c$. Second, the amplitude $w_2 = \beta w_1$ of interlayer hopping that is diagonal in graphene sublattice is measured by the relative strength $\beta \in [0, 1]$ in comparison to off-diagonal hopping. This relative strength is difficult to determine precisely in experiments, being affected by corrugation effects, with typical values evaluated as $\beta \approx 0.82$ [29,30]. Here we keep β as a free parameter. Note that our model thus interpolates between the Bistritzer-MacDonald continuum (BMC) model for $\beta = 1$ [3] and a chirally symmetric continuum (CSC) model for $\beta = 0$ [6].

Following Ref. [3], we use a rotated basis where the Dirac cones $\mathbf{K}_{t,b}$ of the two layers have the *same* (k_x, k_y) coordinates in the mBZ, and measure all energies in units of E_c (see Appendix A for details). The effective Hamiltonian then reads $H'_0 = H_0 + H_\alpha$ with

$$H_0 = i(\boldsymbol{\sigma} \cdot \boldsymbol{\partial})\tau_0, \quad H_\alpha = \alpha \sum_{j=1}^3 e^{-i\mathbf{q}_j \cdot \mathbf{r}} T_j^+ + \text{H.c.}, \quad (1)$$

where $\boldsymbol{\partial} = (\partial_x, \partial_y)$ and the hopping matrices T_j^+ are

$$T_j^+ = (\beta \sigma_0 + e^{i(j-1)2\pi/3} \sigma_+ + e^{-i(j-1)2\pi/3} \sigma_-)\tau_+. \quad (2)$$

Here we introduced two sets of Pauli matrices, σ and τ , which describe respectively the sublattice and layer sectors, with $\sigma_z = \pm 1 = \text{A/B}$ and $\tau_z = \pm 1 = \text{top/bottom}$.

The low-energy physics of this model is nontrivial even without interactions. Indeed, the interlayer couplings prohibit diagonalizing H'_0 . This forbids the use of a simple effective theory valid for all twisting angles θ in the vicinity of the magic values. As a result, we resort to a free electron model in which interlayer hopping effects are accounted for by a self-energy, which is calculated in a perturbative expansion in α . Denoting G'_0 and Σ the translationally-invariant components of the propagator corrected by interlayer hoppings and the self-energy respectively, we have $(G'_0)^{-1} = H_0 - \partial_\tau - \Sigma \approx N_\psi [v(\alpha, \beta) i(\boldsymbol{\sigma} \cdot \boldsymbol{\partial})\tau_0 - \partial_\tau]$, where ∂_τ represents the partial derivative with respect to imaginary time, N_ψ is a wavefunction normalization and $v(\alpha, \beta)$ the Fermi velocity renormalized by the hopping processes (see Appendix B). An expansion to order 6 in α but exact in β , diagrammatically

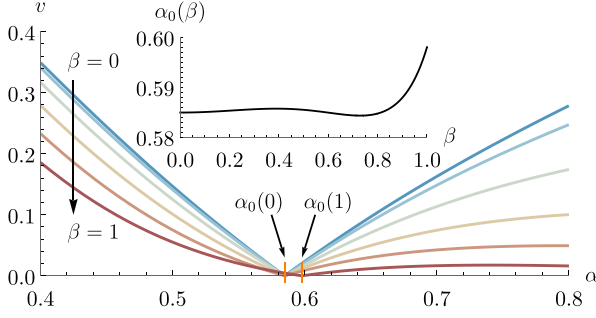


FIG. 3. Fermi velocity $v(\alpha, \beta)$ renormalized by interlayer hoppings at order α^6 , as a function of the relative strength α of the hopping amplitude with respect to the kinetic energy. As the twist angle increases, so does α , and the renormalized velocity vanishes at the first magic angle encoded in the first magic value $\alpha_0(\beta)$ where β sets the asymmetry between diagonal and off-diagonal in sublattice hoppings. Inset: $\alpha_0(\beta)$ depends weakly on corrugation effects, i.e., on the value of β .

represented in Fig. 2, leads to

$$N_\psi v(\alpha, \beta) = 1 - 3\alpha^2 + \alpha^4(1 - \beta^2)^2 - \frac{3}{49}\alpha^6(37 - 112\beta^2 + 119\beta^4 - 70\beta^6). \quad (3)$$

We call $\alpha_0(\beta)$ the lowest value of α for which this Fermi velocity vanishes, which sets the first magic angle value to be approximately 1.1° . As shown in Fig. 3, this first magic value depends weakly on the parameter β , and thus on corrugation, and ranges from $\alpha_0(1) = 0.598$ for the BMC model to $\alpha_0(0) = 0.585$ for the CSC model. These constitute our first results.

III. SYMMETRY-ALLOWED INTERACTIONS

We now identify all short-ranged interaction potentials allowed by the symmetries of the model. In order to do so we turn to a field theoretic formalism and consider the Euclidean action, $S = S'_0 + S_{\text{int}}$, written as a sum of the free electron term

$$S'_0 = \int d^2r d\tau \psi^\dagger (H'_0 - \partial_\tau) \psi, \quad (4)$$

and an interaction term S_{int} , which includes generic local quartic couplings between the fermionic fields ψ^\dagger and ψ . Using group theoretic methods, detailed in Appendix C, we identify all couplings allowed by the symmetries of the low energy model (1) [31]. This amounts to identifying scalar invariants built as direct products of irreducible representations of the corresponding symmetry group. We find that the allowed couplings are (i) 8 channels originating from one-dimensional (1d) corepresentations; and (ii) 4 channels originating from 2d corepresentations:

$$S_{\text{int}} = - \sum_{i=1}^8 g_i \int d^2r d\tau \rho^{(i)}(\mathbf{r}) \rho^{(i)}(\mathbf{r}) - \sum_{j=1}^4 \lambda_j \int d^2r d\tau \mathbf{J}^{(j)}(\mathbf{r}) \cdot \mathbf{J}^{(j)}(\mathbf{r}), \quad (5)$$

TABLE I. One-dimensional (top) and two-dimensional (bottom) corepresentations (corep.) of the magnetic symmetry group of the continuum model, with their associated coupling matrices $\hat{R}^{(i)}$ and $\hat{M}^{(j)}$ expressed in terms of the Pauli matrices in sublattice (σ) and layer (τ) subspaces. These coupling matrices are normalized such that $\text{Tr}[\hat{M}^{(j)} \cdot (\hat{M}^{(j)})^\dagger] = \text{Tr}[\hat{R}^{(i)} \cdot (\hat{R}^{(i)})^\dagger] = 4$. Each one-dimensional corep. can either preserve (\checkmark) or break the combination of inversion and time-reversal symmetries IT , the mirror symmetry C_2 , and the particle-hole antisymmetry P , while preserving the threefold rotational symmetry C_3 . The \pm exponents label the eigenvalue of the IT symmetry.

Corep.	A_1^+	a_1^+	A_2^+	a_2^+	A_1^-	a_1^-	A_2^-	a_2^-
$\hat{R}^{(i)}$	$\sigma_0 \tau_0$	$\sigma_0 \tau_x$	$\sigma_0 \tau_z$	$\sigma_0 \tau_y$	$\sigma_z \tau_y$	$\sigma_z \tau_z$	$\sigma_z \tau_x$	$\sigma_z \tau_0$
IT	\checkmark	\checkmark	\checkmark	\checkmark				
C_2	\checkmark	\checkmark			\checkmark	\checkmark		
P		\checkmark		\checkmark		\checkmark		\checkmark
Corep.	E_2^+		E_4^+		E_2^-		E_4^-	
$\sqrt{2} \hat{M}^{(j)}$	$\sigma \tau_0$		$\sigma \tau_x$		$\sigma \tau_y$		$\sigma \tau_z$	

where the densities $\rho^{(i)}(\mathbf{r}) = \psi^\dagger R^{(i)}(\mathbf{r}) \psi$ and currents $\mathbf{J}^{(j)}(\mathbf{r}) = \psi^\dagger M^{(j)}(\mathbf{r}) \psi$ involve coupling matrices $R^{(i)}(\mathbf{r})$ and $M^{(j)}(\mathbf{r})$. Following our choice of coordinates for the fields in Eq. (1), the coupling matrices in the rotated basis, which enter Eq. (5), are obtained through $R^{(i)} = A(\mathbf{r}) \hat{R}^{(i)} A^\dagger(\mathbf{r})$ and $M^{(j)} = A(\mathbf{r}) \hat{M}^{(j)} A^\dagger(\mathbf{r})$, where $A(\mathbf{r})$ is the transformation matrix of the field (see Appendix A). The coupling matrices $\hat{R}^{(i)}$ and $\hat{M}^{(j)}$ are provided in Table I. The couplings g_i and λ_j are the amplitudes associated with the corresponding coupling potentials.

The moiré pattern is invariant under four discrete ‘‘symmetries’’: (i) the $2\pi/3$ rotation $C_3 = e^{2i\pi/3\sigma_z} \tau_0$ around the z axis orthogonal to the bilayer together with (ii) the π rotation $C_2 = \sigma_x \tau_x$ around the x axis of Fig. 1 generate the point group D_3 , (iii) the composition $IT = \sigma_x \tau_0 \mathcal{K}$ of inversion and time reversal is an antiunitary symmetry, where \mathcal{K} denotes complex conjugation, and (iv) the unitary particle-hole antisymmetry [32] $P = \sigma_x \tau_z$, which satisfies $\{P, H'_0\} = 0$ [33]. The group generated by D_3 and P comprises all unitary operations that leave the Hamiltonian invariant up to a sign. We refer to this ensemble as the *unitary* group \tilde{D}_3 of the model. It can be decomposed into the semidirect product $\tilde{D}_3 = \{e, P, \bar{e}, \bar{P}\} \times D_3$, where $e = \sigma_0 \tau_0$ is the identity operation, $\bar{e} = (PC_2)^2 = -e$ and $\bar{P} = \bar{e}P$. The dichromatic magnetic group \mathcal{M} generated by \tilde{D}_3 and IT can be written as the direct product $\mathcal{M} = \tilde{D}_3 \times \{e, IT\}$. Using the Schur-Frobenius criterion [34–39], we determine the corepresentations (corep.) of \mathcal{M} from the irreducible representations of \tilde{D}_3 , which can be constructed from that of D_3 by induction and basic properties of linear representation theory (see Appendix C).

We combine the resulting coupling matrices of Table I into three sets. The eight interactions originating from 1d coreps. correspond to the density-density couplings diagonal in sublattice while preserving C_3 . Out of these eight couplings, (i) the four interactions associated with 1d coreps. which preserves IT are those symmetric on the A/B sublattices, of the form $(\psi^\dagger \sigma_0 \tau_\mu \psi)(\psi^\dagger \sigma_0 \tau_\mu \psi)$ for $\mu = 0, x, y, z$ [40]. They are distinguished by their breaking of C_2 or P symmetries. (ii)

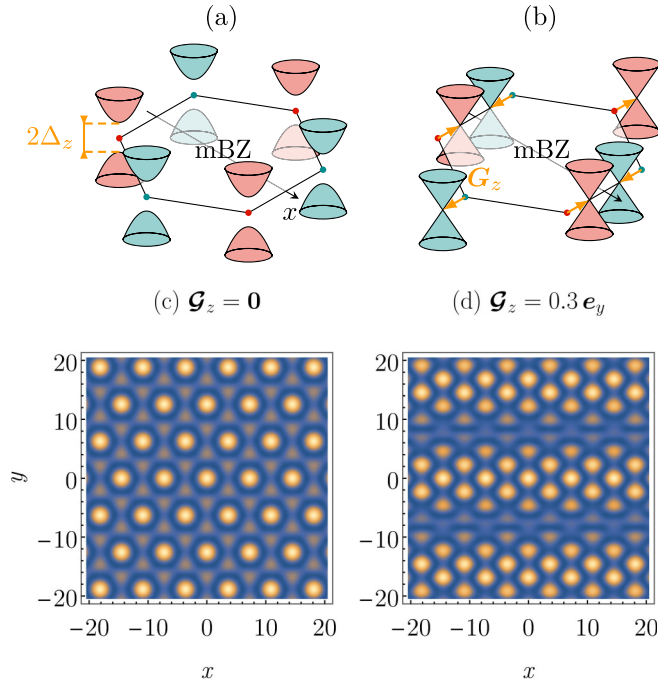


FIG. 4. Schematic dispersion relation of (a) a gapped layer-polarized correlated phase and (b) a density modulated phase. While the gapped phase is characterized by the amplitude of the gap Δ_z opening at the \mathbf{K}_t and \mathbf{K}_b Dirac points, the second phase is characterized by a shift of these Dirac points of amplitude \mathcal{G}_z . This shift leads to a modulation of the relative amplitude of wavefunctions between the two layers, revealed in the density $|\psi_t + \psi_b/2|^2$ probed, e.g., by a STM tip located on the top layer. The behavior of this density is shown (c) without any shift and (d) for a shift $\mathcal{G}_z = 0.3e_y$. The spatial C_3 breaking of this phase is clearly manifested by the appearance of stripes for this density, perpendicular to \mathcal{G}_z .

The four interactions associated with 1d coreps., which break IT are those, which are antisymmetric in the A/B sublattices, with couplings of the form $(\psi^\dagger \sigma_z \tau_\mu \psi)(\psi^\dagger \sigma_z \tau_\mu \psi)$. Similarly to set (i), they can break C_2 or P . Finally, the (iii) four interactions originating from 2d coreps. are current-current couplings between the layers, off-diagonal in sublattices, of the form $(\psi^\dagger \sigma \tau_\mu \psi) \cdot (\psi^\dagger \sigma \tau_\mu \psi)$. They break all symmetries of the free model, and in particular the threefold rotational symmetry C_3 .

IV. NATURE OF THE CORRELATED PHASES

Let us first discuss the nature of the phases induced by these couplings. The interactions of type (i), symmetric in sublattices, neither open a gap at the Dirac point nor induce a density modulation. On the other hand, interactions of type (ii) generate phases with a gap $\Delta_\mu \propto g_\mu \langle \psi^\dagger \sigma_z \tau_\mu \psi \rangle$, reminiscent of the gap opening in boron nitride, see Fig. 4(a). These various gapped phases are distinguished by their layer correlations. Current-current interactions of type (iii) lead to radically different phases, in which the Dirac cones of the two layers are shifted with respect to each other by a momentum $2\mathcal{G}_\mu \propto \lambda_\mu \langle \psi^\dagger \sigma \tau_\mu \psi \rangle$, as shown in Fig. 4(b). They generate gapless phases with C_3 -breaking density modulations. These spatial modulations are detected when probing the electronic density

from one side of the bilayer, which amounts to coupling the local probe asymmetrically to the top and bottom wavefunctions, thus scanning some interlayer density of the form $|\psi_t + r\psi_b|^2$, where $0 < r < 1$ is the asymmetry parameter. In Fig. 4 we compare the corresponding density for an asymmetry $r = 1/2$ in the absence of any instability in Fig. 4(c) with that in the presence of a C_3 -breaking instability in Fig. 4(d). Stripe-like modulations of the interlayer-correlated density are readily observed in this last case.

To gain further insight into the behavior of these phases close to the first magic angle, we now study their mean-field behavior. As we will show later using a renormalization group analysis, only four out of the twelve couplings are sensitive to the proximity of the magic angle. They correspond to the interaction potentials diagonal in layers, and originate from the a_1^-, a_2^- coreps. of set (ii) with respective amplitude g_z, g_0 , and the E_4^-, E_2^+ coreps. of set (iii) with amplitudes λ_0, λ_z . The corresponding order parameters satisfy the self-consistency equations [41]

$$\Delta_{0/z} = -2g_{0/z} \int d\omega \int_{\Lambda} \frac{d^2q}{(2\pi)^3} \langle \psi_{q,\omega}^\dagger \sigma_z \tau_{0/z} \psi_{q,\omega} \rangle, \quad (6a)$$

$$\mathcal{G}_{0/z} = -2\lambda_{0/z} \int d\omega \int_{\Lambda} \frac{d^2q}{(2\pi)^3} \langle \psi_{q,\omega}^\dagger \sigma \tau_{0/z} \psi_{q,\omega} \rangle. \quad (6b)$$

The correlators in Eq. (6) are the translationally-invariant parts of statistical averages computed over the Bloch Hamiltonian density $H'_{\text{MF}} = H'_0 + \sigma \cdot (\mathcal{G}_0 \tau_0 + \mathcal{G}_z \tau_z) + \sigma_z (\Delta_0 \tau_0 + \Delta_z \tau_z)$. The corrections by interlayer hoppings of the correlators in Eq. (6) are obtained within a perturbation expansion in α . Incorporating the hoppings H_α leads to an enhancement of the order parameters by factors $N_{0/z}^{(\mathcal{G}/\Delta)}(\alpha, \beta)$, as is the case for the renormalization of the Fermi velocity; they are calculated diagrammatically to sixth order in α in Appendix D. The resulting dependence of each separate order parameter on the proximity to the magic angle and for various strengths of the couplings is depicted in Fig. 5. The insulating phases, characterized by a gap Δ_0 or Δ_z , develop at a critical coupling, which decreases as the parameter α approaches its magic value α_0 . Such gapped phases generically occur in some range of twist angles around the magic value, in agreement with the experimental findings of Ref. [42]. At the mean-field level and for a fixed α , we find that a Δ_0 insulator occurs for weaker couplings g_0 than the couplings g_z required for the appearance of the Δ_z insulator. We will see that this hierarchy is modified when fluctuations are accounted for, demonstrating the necessity to develop the RG approach. The situation for the C_3 symmetry breaking phases with periodic modulation is different: While the phase, which is antisymmetric in layers, characterized by a \mathcal{G}_z momentum, is also favored by the vanishing bandwidth close to α_0 , the finite critical strength for the analogous phase symmetric in layer, associated with \mathcal{G}_0 , does not depend on α .

By considering the interactions allowed by symmetries we identified all possible instabilities of TBG. While the mean-field approximation and related analysis discussed in this section allowed us to understand the physical meaning of these instabilities and investigate the behavior of the order parameters close to the magic angle, mean field cannot be trusted on large scale, nor can it capture accurately the

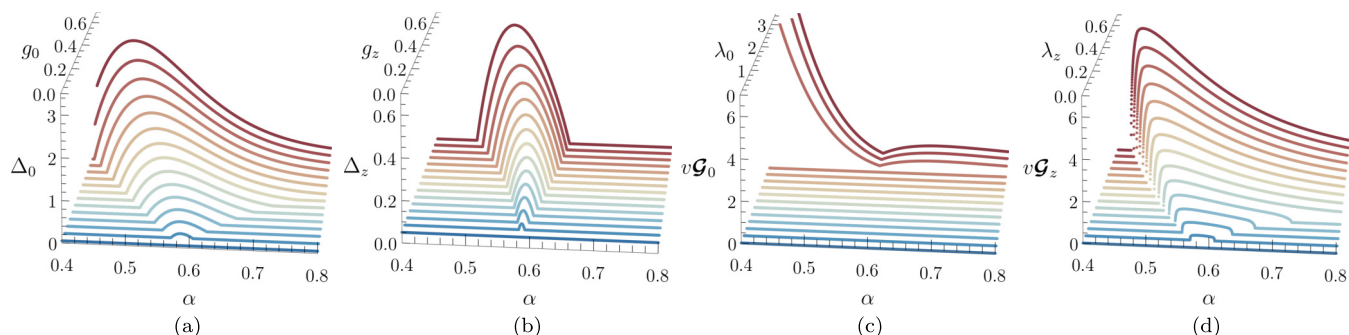


FIG. 5. Mean-field order parameters of the leading instabilities as a function of the twisting angle encoded in α and for various coupling strengths. Layer-polarized gap Δ_z (a) and Δ_0 (b). [(c),(d)] Energy $v\mathcal{G}_z$ and $v\mathcal{G}_0$ of the layer-polarized density modulated phase associated to shift \mathcal{G}_z and \mathcal{G}_0 of the Dirac cones (here the shifts are oriented along the y axis). The amplitudes of the order parameters are provided for $\beta = 0.82$ and in arbitrary units of $10^{-2}\Lambda$ where Λ is an energy cut-off.

competition between the instabilities since it neglects quantum fluctuations. The standard technique to handle these fluctuations is the renormalization group approach, which has been largely developed to study various competing instabilities of interacting fermions [43,44].

V. RENORMALIZATION GROUP PICTURE

As we have seen, the vanishing of the kinetic energy scale set by the renormalized velocity v entails that the four nontrivial interactions are relevant close to the first magic angle. In order to identify the leading instability, we study via a RG approach the competition between them as α approaches the first magic value. Our starting point is the field theory described by the action $S = S'_0 + S_{\text{int}}$ where the quadratic action S'_0 given in Eq. (4) involves both the kinetic energy and the interlayer hoppings. We sum over the latter to capture the vanishing energy scale. Hence, we expand the correlation functions of the interacting theory not only in the coupling constants but also in the amplitude of interlayer hoppings.

Motivated by the experimental observations of an insulating behavior at charge neutrality, we carry out a “particle-hole” Hubbard-Stratonovich transformation suitable to describe gapped phases (as opposed to superconductors). We introduce the scalar bosonic fields ϕ_i , $i = 1, \dots, 8$ for each 1d channel and the vector bosonic fields φ_j , $j = 1, \dots, 4$ for each 2d channel, so that the interaction part of the action (5) becomes

$$S_{\text{int}} \rightarrow \sum_{i=1}^8 \int d^{d-1}r d\tau (\phi_i^2 + 2\sqrt{g_i} \phi_i \psi^\dagger R^{(i)}(\mathbf{r})\psi) + \sum_{j=1}^4 \int d^{d-1}r d\tau (\varphi_j^2 + 2\sqrt{\lambda_j} \varphi_j \cdot \psi^\dagger \mathbf{M}^{(j)}(\mathbf{r})\psi). \quad (7)$$

We expand around the lower critical dimension, setting the space-time dimension to $d = 2 + \epsilon$, and renormalize the theory using the minimal subtraction scheme. We introduce the renormalized couplings $\hat{g} \in \{g_i, \lambda_j\}$ related to the bare ones by $\hat{g} = \mu^{-\epsilon} N_\psi^2 Z_g^2 Z_\phi^{-1} g$. Here μ is the momentum scale at which we renormalize the theory and N_ψ is the wavefunction

normalization factor generated by interlayer hoppings, which was introduced previously. The renormalization constants Z_g and Z_ϕ for $\phi \in \{\phi_i, \varphi_j\}$ absorb the poles of the three-point vertex and the bosonic self-energy, respectively. We expand these functions to first order in the interaction couplings using the Green’s function corrected by interlayer hoppings G'_0 as the fermionic propagator. This expansion is represented by the diagrams shown in Fig. 6, where interlayer hoppings are treated perturbatively to second order in α . We obtain the RG flow equations for the coupling constants as a function of the parameters α and β . Crucially, we find that only four interactions out of twelve have nonzero divergent corrections. The eight other couplings have a trivial flow, either because the correction has no pole in ϵ —these correspond to the four channels with σ_0 sublattice structure; or because the correction vanishes at low energy—these correspond to the four channels that are off-diagonal in layer space. We thus restrict our study to the four-dimensional subspace corresponding to the instabilities of Table II, which are all associated with a

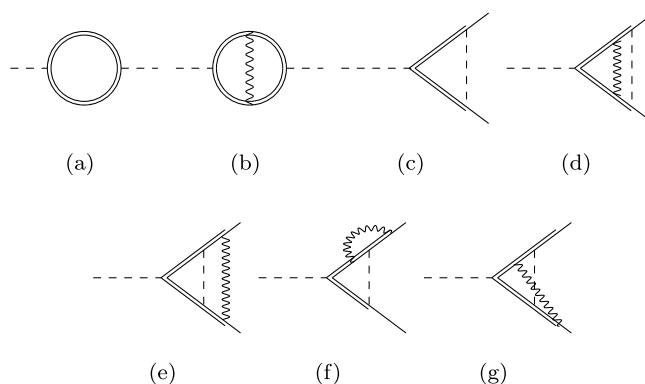


FIG. 6. [(a),(b)] Polarization (bosonic self-energy) to first order in the couplings, (a) at order α^0 and (b) at order α^2 . [(c)–(g)] Three-point vertex to first order in the couplings, (c) at order α^0 ; [(d),(e)] at order α^2 with multiplicity one; [(f),(g)] at order α^2 with multiplicity two. The double line is the fermionic propagator corrected by interlayer hoppings, while the dashed line is the bosonic propagator. The wavy line represents a pair of opposite hopping processes, summed over all channels with a transfer of momentum $\pm\mathbf{q}_j$ for $j = 1, 2, 3$.

TABLE II. Isolated, non-Gaussian critical fixed points (FPs) for the four nontrivial instabilities.

Channel	Coupling	\hat{M}_i	FP $g_i^*(\alpha, \beta)$
a_2^-	g_0	$\sigma_z \tau_0$	$\pi v \epsilon / (4[1 - 12\alpha^2(1 - \beta^2)])$
a_1^-	g_z	$\sigma_z \tau_z$	$\pi v \epsilon / 4$
E_2^+	λ_0	$\sigma \tau_0 / \sqrt{2}$	$\pi v \epsilon / (4[1 - 3\alpha^2(1 - \beta^2)])$
E_4^-	λ_z	$\sigma \tau_z / \sqrt{2}$	$\pi v \epsilon / (4[1 + 3\alpha^2(1 + \beta^2)])$

phase transition toward a correlated phase. These relevant couplings are all diagonal in layer. We now briefly discuss the essential features of this four-dimensional flow. The Gaussian fixed point (FP) at the origin is always stable in $d = 3$. Besides, we identify four critical points, one for each nontrivial coupling, listed in Table II. They control phase transitions toward the four correlated phases discussed in the mean-field analysis. As α approaches the magic value α_0 , all four critical FPs collapse towards the Gaussian FP, *independently of the value of the control parameter* ϵ , which only appears together with a factor of v . Meanwhile, the (Dirac) semimetallic region, which corresponds to the basin of attraction of the Gaussian FP, shrinks and disappears completely. As a result, these four couplings are always relevant close enough to the magic angle, regardless of the value of the bare interaction strength. This scenario, which becomes *more* controlled near the magic angle, provides a natural way of identifying the dominant instabilities near the magic angle: they correspond to the couplings whose critical FPs collapse the fastest towards the origin.

Hence, as follows from Table II, we discard the couplings g_0 and λ_0 (the amplitudes of interactions, which are symmetric in layers) and focus on the competition between the couplings, which are antisymmetric in layers, of amplitude g_z associated with the layer-polarized gapped phase and λ_z associated with the C_3 -breaking density-modulated phase. This hierarchy of instabilities differs from the results of the mean-field (MFT) analysis of Sec. IV, where we found that, within MFT, a layer-symmetric gap develops on a larger region of twist angle than its layer-antisymmetric counterpart. This difference highlights the crucial effects of quantum fluctuations. We note that, while the gapped phase is reminiscent of the dynamical mass generation in the Gross-Neveu model [45,46], the C_3 -breaking density-modulated phase is specific to TBG. The competition between the two most relevant instabilities is dictated by the following coupled RG flows (for derivation see Appendix E)

$$-\mu \frac{\partial g_z}{\partial \mu} = -\epsilon g_z + \frac{4g_z^2}{\pi v} + \frac{4g_z \lambda_z}{\pi v} [1 - 6\alpha^2(1 - \beta^2)], \quad (8)$$

$$-\mu \frac{\partial \lambda_z}{\partial \mu} = -\epsilon \lambda_z + \frac{4\lambda_z^2}{\pi v} [1 + 3\alpha^2(1 + \beta^2)] + \frac{2\lambda_z g_z}{\pi v} [1 - 6\alpha^2(1 - \beta^2)]. \quad (9)$$

As mentioned above, all FPs collapse to the origin at the magic angle. Thus to explore the competition between the phases, we plot the renormalization flow for the couplings rescaled by the vanishing velocity. The effect of the proximity to the magic angle on this competition is shown in Fig. 7, where we

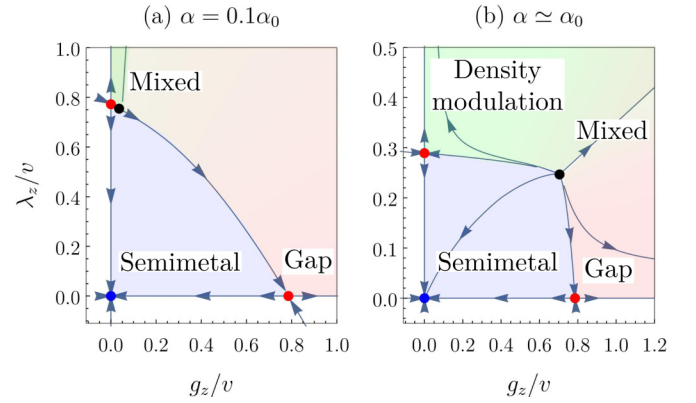


FIG. 7. Renormalization flow of the couplings g_z and λ_z at $\beta = 0.82$ [29,30], (a) for a weak interlayer hopping amplitude, $\alpha = 0.1\alpha_0$; and (b) close to the first magic angle, $\alpha \simeq \alpha_0$. As α approaches α_0 , the blue semimetal region shrinks to the origin. To study the competition between the couplings we rescale them by the vanishing velocity v . The red critical FPs control the transitions toward the gapped (red region) or density-modulated (green region) phases. The black source FP gives rise to a crossover region (mixed state). It migrates away from the vertical axis as we increase α , thus expanding the density-modulated region.

compare the flow close to the first magic angle (b) with that for the case when interlayer hopping is suppressed (a) [47]. This comparison shows that the proximity to the magic angle favors the occurrence of density modulations. The large scale behavior is dominated by the fastest diverging coupling, whether g_z or λ_z . Within our perturbative RG analysis, a crossover line separates the corresponding regions, whose parametric equation reads $\lambda_z = g_z [1 + 6\alpha^2(1 - \beta^2)] / [6\alpha^2(3 - \beta^2)]$. Around the crossover line, both order parameters coexist over a large range of length scales, corresponding to the appearance of a gapped, periodically modulated state, asymmetric in layers and breaking the C_3 and IT symmetries. We call it a nematic insulator by analogy with phases discussed in Ref. [48]. This nematic insulating behavior is characterized by a runaway RG flow of both λ_z, g_z . While the asymptotic behavior of such a runaway flow cannot be quantitatively described by the perturbative RG technique we developed, the latter is known to generally successfully capture the nature of the corresponding emerging phase [43,44]. Moreover, the appearance of a runaway flow accurately captures the existence of the instability over a wide range of coupling parameters in the proximity of the magic angle.

VI. DISCUSSION AND OUTLOOK

Applying group theory supplemented by a renormalization group approach, our paper concludes that the proximity to the first magic angle in TBG favors a gapped nematic state at charge neutrality. Within a valley polarized assumption, we have identified the associated order parameter whose spatial correlations display C_3 breaking modulations. A gap as in our nematic state at charge neutrality was experimentally observed both in scanning tunneling microscopy studies [14,24,25,49] as well as in four-terminal transport measurements [23]. Similarly, nematic ordering, or threefold

symmetry breaking, was reported in [22,24,25]. All of these experimental observations strongly support the occurrence of a nematic insulating state at charge neutrality in TBG, as we identify in our study. Furthermore, our analysis is fully consistent with the robustness of this state to a weakening of the interactions as was experimentally demonstrated in Ref. [50]. While the appearance of such a nematic gapped phase was previously theoretically viewed as an *explicit* C_3 symmetry breaking effect [51], we have identified an *intrinsic* mechanism relying on quantum fluctuations and captured within the renormalization group formalism.

Finally we note that our RG approach reveals a gapped nematic behavior in the perturbative scaling regime, but does not rule out that other correlations develop at much smaller length scales, including those of intervalley-coherent and generalized-ferromagnetic insulating states recently discussed in Refs. [52–56]. While our valley-symmetric assumption can be viewed as a mean-field treatment of such perturbations occurring on smaller scales, incorporating intervalley correlations into a full RG treatment would drastically complicate calculations. Nevertheless, we believe that our results, which show that two out of twelve intravalley couplings become most important, provide a natural starting point to incorporate these additional interactions.

The energies of these ground states seem to be very close to each other, suggesting a strong sensitivity to experimental conditions [56]. Finally, the occurrence of an analogous nematic insulating state close to quantum spin Hall phase transitions raises the questions of its relation with the topological nature of the underlying semimetal [33,51,57].

ACKNOWLEDGMENTS

We would like to thank Leon Balents for valuable discussions. We acknowledge support from the French Agence Nationale de la Recherche through Grant No. ANR-17-CE30-0023(DIRAC3D), the ToRe IdexLyon breakthrough program, and funding from the European Research Council (ERC) under the European Union’s Horizon 2020 research and innovation program (Grant Agreement No. 853116, “TRANSPORT”).

APPENDIX A: CHANGE OF BASIS

The Hamiltonian describing the low-energy physics near the two twisted Dirac cones at $\mathbf{K}_{t,b}$ originating from a single valley of graphene can be written as [58]

$$\hat{H} = \int d^2r \hat{\psi}^\dagger \begin{pmatrix} v_0 \boldsymbol{\sigma} \cdot (i\partial + \frac{\mathbf{q}_1}{2}) & \hat{T}^\dagger(\mathbf{r}) \\ \hat{T}(\mathbf{r}) & v_0 \boldsymbol{\sigma} \cdot (i\partial - \frac{\mathbf{q}_1}{2}) \end{pmatrix} \hat{\psi}. \quad (\text{A1})$$

The momentum $\mathbf{q}_1 = \mathbf{K}_t - \mathbf{K}_b$ gives the relative displacement of the Dirac momentum \mathbf{K} of each layer due to the twist, while v_0 is the Fermi velocity of graphene. Notice that there are three equivalent \mathbf{K} points in monolayer graphene, each leading to one copy of the Hamiltonian \hat{H} with a relative displacement \mathbf{q}_j , $j = 1, 2, 3$, where the momenta \mathbf{q}_2 and \mathbf{q}_3 are obtained through a rotation of \mathbf{q}_1 by an angle of $2\pi/3$ and

$4\pi/3$ respectively. The interlayer hopping matrix $\hat{T}(\mathbf{r})$ reads

$$\begin{cases} \hat{T}(\mathbf{r}) = \sum_{j=1}^3 e^{-i(\mathbf{q}_j - \mathbf{q}_1) \cdot \mathbf{r}} T_j^+ + \text{H.c.} \\ T_j = \frac{t_{AA}}{3} \sigma_0 + \frac{t_{AB}}{3} (\sigma_+ e^{-2i(j-1)\pi/3} + \text{H.c.}) \end{cases}, \quad (\text{A2})$$

where t_{AA} and t_{AB} are the hopping amplitudes in the AA and AB/BA regions, respectively.

Hamiltonian (A1) is simplified by rotating the basis [3]

$$\hat{\psi}(\mathbf{r}, \tau) = A_1(\mathbf{r}) \psi(\mathbf{r}, \tau), \quad A_j(\mathbf{r}) = e^{-i(\mathbf{q}_j \cdot \mathbf{r}/2) \tau}, \quad (\text{A3})$$

which brings the Dirac cones to the same momentum,

$$H = \int d^2r \psi^\dagger \begin{pmatrix} v_0 \boldsymbol{\sigma} \cdot i\partial & T^\dagger(\mathbf{r}) \\ T(\mathbf{r}) & v_0 \boldsymbol{\sigma} \cdot i\partial \end{pmatrix} \psi, \quad (\text{A4})$$

where $T(\mathbf{r}) = \sum_{j=1}^3 e^{-i\mathbf{q}_j \cdot \mathbf{r}} T_j^+$. Applying the same change of basis to quartic terms in the action, e.g., corresponding to a density-density interaction of the form

$$S_{\text{int}} = g \int d^2r d\tau \hat{\psi}^\dagger(\mathbf{r}, \tau) \hat{R} \hat{\psi}(\mathbf{r}, \tau) \hat{\psi}^\dagger(\mathbf{r}, \tau) \hat{R} \hat{\psi}(\mathbf{r}, \tau), \quad (\text{A5})$$

we arrive at

$$S_{\text{int}} = g \int d^2r d\tau \psi^\dagger(\mathbf{r}, \tau) R(\mathbf{r}) \psi(\mathbf{r}, \tau) \psi^\dagger(\mathbf{r}, \tau) R(\mathbf{r}) \psi(\mathbf{r}, \tau) \quad (\text{A6})$$

with the rotated interaction matrix

$$R(\mathbf{r}) = \frac{1}{3} \sum_{j=1}^3 A_j^\dagger(\mathbf{r}) \hat{R} A_j(\mathbf{r}). \quad (\text{A7})$$

Though both \hat{R} and $R(\mathbf{r})$ describe contact interactions, while \hat{R} is space independent, $R(\mathbf{r})$ depends in general on the position as a consequence of Eq. (A7).

(i) If \hat{R} is diagonal in layer, i.e., proportional to $\tau_{0/z}$, it commutes with $A_j(\mathbf{r})$ so that $R(\mathbf{r}) = \hat{R}$.

(ii) If \hat{R} is not diagonal in layer, i.e., proportional to $\tau_{x/y}$, it does not commute with $A_j(\mathbf{r})$ so that $R(\mathbf{r})$ differs from \hat{R} . In that case, $R(\mathbf{r})$ is modulated periodically over a distance of the order of the moire lattice constant. Indeed, we have

$$\begin{cases} \frac{1}{3} \sum_{j=1}^3 A_j^\dagger(\mathbf{r}) \tau_x A_j(\mathbf{r}) = f_1(\mathbf{r}) \tau_x + f_2(\mathbf{r}) \tau_y \\ \frac{1}{3} \sum_{j=1}^3 A_j^\dagger(\mathbf{r}) \tau_y A_j(\mathbf{r}) = f_2(\mathbf{r}) \tau_x + f_1(\mathbf{r}) \tau_y \end{cases}, \quad (\text{A8})$$

with $f_1(\mathbf{r}) = \frac{1}{3} \sum_{j=1}^3 \cos(\mathbf{q}_j \cdot \mathbf{r})$, $f_2(\mathbf{r}) = \frac{1}{3} \sum_{j=1}^3 \sin(\mathbf{q}_j \cdot \mathbf{r})$. These results also apply to current-current quartic interactions, where \hat{R} is replaced by a vector of matrices $\hat{\mathbf{M}}$.

APPENDIX B: DIAGRAMMATIC TECHNIQUE FOR THE NONINTERACTING THEORY

To expand any observable in interlayer hoppings in the absence of interactions, it is not mandatory to resort to a field theoretical approach. We do so however, because it is

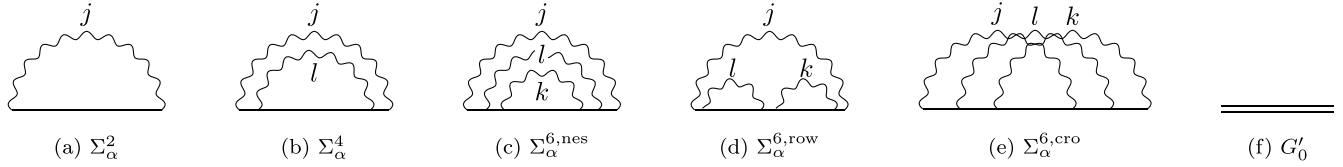


FIG. 8. Translational invariant part of the self-energy, $\Sigma_\alpha(\mathbf{k}, \Omega)$, at order (a) α^2 , (b) α^4 , and [(c)–(e)] α^6 . At order six, the hopping (wavy lines can be (c) nested, (d) in a row, or (e) crossed. Interlayer hoppings are summed over up to three momenta denoted generically as $\mathbf{q}_j, \mathbf{q}_l$, and \mathbf{q}_k , with $j, l, k = 1, 2, 3$. The straight-solid lines represent the fermionic propagator of the decoupled bilayer, $G_0(\mathbf{k}, \Omega)$, given by Eq. (B1). (f) Translational invariant part of the fermionic propagator corrected by interlayer hopping, $G'_0(\mathbf{k}, \Omega)$, given by Eq. (B11).

useful for applying RG when interactions are included. To that end we need to introduce the Feynman rules specific to this unusual field theory. The free fermionic propagator associated to the action of the decoupled bilayer $S_0 = \int d^2r d\tau \psi^\dagger (H_0 - \partial_\tau) \psi$ reads

$$G_0(\mathbf{k}, \Omega) = (\boldsymbol{\sigma} \cdot \mathbf{k} - i\Omega)^{-1} \quad (\text{B1})$$

in Fourier space, where \mathbf{k} is the momentum, Ω the Matsubara frequency, and we omitted the identity matrices σ_0 and τ_0 for simplicity. When drawing Feynman diagrams, we represent the free propagator (B1) with a solid line. We reserve \mathbf{q} and ω for the internal momentum and Matsubara frequency and use \mathbf{k} and Ω for external ones. Any correlation function can be written as an ensemble average $\langle \dots \rangle_0$ over S_0 . In particular for the time-ordered two-point function we have

$$\langle \mathcal{T} \psi \psi^\dagger \rangle'_0 = \frac{\langle \mathcal{T} \psi \psi^\dagger e^{-S_\alpha} \rangle_0}{\langle e^{-S_\alpha} \rangle_0}, \quad (\text{B2})$$

where $\langle \dots \rangle'_0$ denotes the ensemble average over the quadratic action $S'_0 = S_0 + S_\alpha$, which includes the hopping action $S_\alpha = \int d^2r d\tau \psi^\dagger H_\alpha \psi$, from which an expansion order by order in α can be carried out. The two-point function (B2) is nondiagonal in momentum space, since S_α reduces the continuous translational symmetry to the discrete translational symmetry over the reciprocal lattice \mathcal{R} , which is the \mathbb{Z} -module generated by the (linearly dependent) family of vectors $\{\mathbf{q}_j, j = 1, 2, 3\}$. For every vector \mathbf{b} in \mathcal{R} , we define the component $G'_0(\mathbf{b}, \mathbf{k}, \Omega)$ of the two-point function such that

$$\langle \mathcal{T} \psi_{\mathbf{k}, \Omega} \psi^\dagger_{\mathbf{k}+\mathbf{q}, \Omega} \rangle'_0 = \sum_{\mathbf{b} \in \mathcal{R}} G'_0(\mathbf{b}, \mathbf{k}, \Omega) \delta(\mathbf{b} - \mathbf{q}), \quad (\text{B3})$$

for all momenta \mathbf{k}, \mathbf{q} and frequency Ω . We focus on how interlayer hoppings renormalize the dispersion relation, so that we are mainly interested in the translational invariant part $G'_0(\mathbf{k}, \Omega) = G'_0(\mathbf{0}, \mathbf{k}, \Omega)$ of the fermionic propagator, represented in Fig. 8(f) as a double line. Successive interlayer hoppings that transfer the momenta $(\eta_1 \mathbf{q}_{j_1}, \dots, \eta_m \mathbf{q}_{j_m})$ in this precise order—where $\eta_1, \dots, \eta_m = \pm$, with the plus sign for a hopping to the top layer, and a minus sign to the bottom layer—give a nonzero contribution to $G'_0(\mathbf{k}, \Omega)$ if the following conditions are met.

- (i) Total momentum is conserved, i.e., $\sum_{r=1}^m \eta_r \mathbf{q}_{j_r} = \mathbf{0}$.
- (ii) Consecutive hopping processes affect different layers, i.e., $\eta_{2r} = -\eta_{2r-1}$ for all $r = 1, \dots, n/2$.

In particular, condition (ii) forbids odd numbers of insertions, so that all correlation functions can be expanded in α^2 ,

and entails that a hopping sequence is determined by the momenta and the sign of only the first hopping process $\eta = \eta_1$. Joined with condition (i), it also yields that the transfer of a momentum at one point of the diagram must be followed by the transfer of the opposite momentum at another point. Thus we can join insertions of opposite momenta by a wavy line like in Figs. 8(a)–8(d).

We now introduce the translational part $\Sigma_\alpha(\mathbf{k}, \Omega)$ of the self-energy as

$$G'_0(\mathbf{k}, \Omega)^{-1} = G_0(\mathbf{k}, \Omega)^{-1} - \Sigma_\alpha(\mathbf{k}, \Omega). \quad (\text{B4})$$

The contributions to $\Sigma_\alpha(\mathbf{k}, \Omega)$ come from the connected two-point diagrams that conserve total momentum and that cannot be cut by one stroke into two subdiagrams that conserve themselves total momentum. Expanding Eq. (B2) to sixth order in α , we can decompose it as $\Sigma_\alpha(\mathbf{k}, \Omega) = \Sigma_\alpha^2(\mathbf{k}, \Omega) + \Sigma_\alpha^4(\mathbf{k}, \Omega) + \Sigma_\alpha^{6,nes}(\mathbf{k}, \Omega) + \Sigma_\alpha^{6,row}(\mathbf{k}, \Omega) + \Sigma_\alpha^{6,cro}(\mathbf{k}, \Omega)$. In the following we use the shortcut $\bar{\eta} = -\eta$ with $\eta = \pm$, and $j, l, k = 1, 2, 3$. The second-order contribution [Fig. 8(a)] reads

$$\Sigma_\alpha^2(\mathbf{k}, \Omega) = \alpha^2 \sum_{\eta, j} T_j^{\bar{\eta}} G_0(\mathbf{k} + \eta \mathbf{q}_j, \Omega) T_j^\eta. \quad (\text{B5})$$

The fourth-order contribution [Fig. 8(b)] reads

$$\begin{aligned} \Sigma_\alpha^4(\mathbf{k}, \Omega) &= \alpha^4 \sum_{\eta, j \neq l} T_j^{\bar{\eta}} G_0(\mathbf{k} + \eta \mathbf{q}_j, \Omega) \\ &\quad \times T_l^\eta G_0(\mathbf{k} + \eta \mathbf{q}_j - \eta \mathbf{q}_l, \Omega) \\ &\quad \times T_l^{\bar{\eta}} G_0(\mathbf{k} + \eta \mathbf{q}_j, \Omega) T_j^\eta. \end{aligned} \quad (\text{B6})$$

The sixth-order contribution splits into three terms. The first diagram hosts three nested hopping lines [Fig. 8(c)],

$$\begin{aligned} \Sigma_\alpha^{6,nes}(\mathbf{k}, \Omega) &= \alpha^6 \sum_{\eta, l \neq (j, k)} T_j^{\bar{\eta}} G_0(\mathbf{k} + \eta \mathbf{q}_j, \Omega) \\ &\quad \times T_l^\eta G_0(\mathbf{k} + \eta \mathbf{q}_j - \eta \mathbf{q}_l, \Omega) \\ &\quad \times T_k^{\bar{\eta}} G_0(\mathbf{k} + \eta \mathbf{q}_j + \eta \mathbf{q}_k - \eta \mathbf{q}_l, \Omega) \\ &\quad \times T_k^\eta G_0(\mathbf{k} + \eta \mathbf{q}_j - \eta \mathbf{q}_l, \Omega) \\ &\quad \times T_l^{\bar{\eta}} G_0(\mathbf{k} + \eta \mathbf{q}_j, \Omega) T_j^\eta. \end{aligned} \quad (\text{B7})$$

The second diagram hosts two hopping lines in a row, embedded in a third one [Fig. 8(d)],

$$\begin{aligned} \Sigma_{\alpha}^{6,\text{row}}(\mathbf{k}, \Omega) &= \alpha^6 \sum_{\eta, j \neq (l, k)} T_j^{\bar{\eta}} G_0(\mathbf{k} + \eta \mathbf{q}_j, \Omega) T_l^{\eta} G_0(\mathbf{k} + \eta \mathbf{q}_j - \eta \mathbf{q}_l, \Omega) T_l^{\bar{\eta}} G_0(\mathbf{k} + \eta \mathbf{q}_j, \Omega) \\ &\quad \times T_k^{\eta} G_0(\mathbf{k} + \eta \mathbf{q}_j - \eta \mathbf{q}_k, \Omega) T_k^{\bar{\eta}} G_0(\mathbf{k} + \eta \mathbf{q}_j, \Omega) T_j^{\eta}. \end{aligned} \quad (\text{B8})$$

The third diagram consists in three crossing hopping lines [Fig. 8(e)],

$$\begin{aligned} \Sigma_{\alpha}^{6,\text{cro}}(\mathbf{k}, \Omega) &= \alpha^6 \sum_{\eta, j \neq l \neq k} T_k^{\bar{\eta}} G_0(\mathbf{k} + \eta \mathbf{q}_k, \Omega) T_l^{\eta} G_0(\mathbf{k} + \eta \mathbf{q}_k - \eta \mathbf{q}_l, \Omega) T_j^{\bar{\eta}} G_0(\mathbf{k} + \eta \mathbf{q}_j + \eta \mathbf{q}_k - \eta \mathbf{q}_l, \Omega) \\ &\quad \times T_k^{\eta} G_0(\mathbf{k} + \eta \mathbf{q}_j - \eta \mathbf{q}_l, \Omega) T_l^{\bar{\eta}} G_0(\mathbf{k} + \eta \mathbf{q}_j, \Omega) T_j^{\eta}. \end{aligned} \quad (\text{B9})$$

Within a low-energy theory where $k, \Omega \ll 1$, we can further expand to order two in momentum \mathbf{k} , and one in Matsubara frequency Ω , which results in

$$\begin{aligned} \Sigma_{\alpha}(\mathbf{k}, \Omega) &= \left[3\alpha^2 - \alpha^4(1 - \beta^2)^2 + \frac{3\alpha^6}{49}(37 - 112\beta^2 + 119\beta^4 - 70\beta^6) \right] \boldsymbol{\sigma} \cdot \mathbf{k} \tau_0 + [3\alpha^2\beta^2 - 9\alpha^4\beta^2(1 - \beta^2)] \begin{pmatrix} 0 & i\mathbf{k}^2 \\ -i\mathbf{k}^{*2} & 0 \end{pmatrix} \tau_z \\ &\quad + \left[3\alpha^2(1 + \beta^2) + 2\alpha^4(1 + 7\beta^2 + 4\beta^4) + \frac{3\alpha^6}{28}(8 + 16\beta^2 + 376\beta^4 + 187\beta^6) \right] i\Omega \sigma_0 \tau_0, \end{aligned} \quad (\text{B10})$$

where $\mathbf{k} = k_x + ik_y$. If one keeps only the correction to the linear dispersion, the translational part of the fermionic propagator corrected by interlayer hoppings can be massaged into

$$G'_0(\mathbf{k}, \Omega) = N_{\psi}^{-1} (v\boldsymbol{\sigma} \cdot \mathbf{k} - i\Omega)^{-1} \quad (\text{B11})$$

with the normalization of the wave function $N_{\psi} = 1 + 3\alpha^2(1 + \beta^2) + 2\alpha^4(1 + 7\beta^2 + 4\beta^4) + \frac{3}{28}\alpha^6(8 + 16\beta^2 + 376\beta^4 + 187\beta^6)$, and the Fermi velocity dressed by interlayer hoppings

$$v = \frac{1 - 3\alpha^2 + \alpha^4(1 - \beta^2)^2 - \frac{3}{49}\alpha^6(37 - 112\beta^2 + 119\beta^4 - 70\beta^6)}{1 + 3\alpha^2(1 + \beta^2) + 2\alpha^4(1 + 7\beta^2 + 4\beta^4) + \frac{3}{28}\alpha^6(8 + 16\beta^2 + 376\beta^4 + 187\beta^6)}, \quad (\text{B12})$$

as given in Eq. (3). We remind that v is expressed in units of the Fermi velocity v_0 of monolayer graphene.

APPENDIX C: SYMMETRIES OF THE MODEL

1. Complete symmetries

The symmetries of the single-particle Hamiltonian $H'_0 = H_0 + H_{\alpha}$ of Eq. (1) are highly constrained by the interlayer hopping term. Indeed, the Hamiltonian of the decoupled bilayer $H_0 = i\boldsymbol{\sigma} \cdot \boldsymbol{\partial} \tau_0$, is invariant under the layer pseudospin rotational group $U(1)$, and the Poincaré group $\mathbb{R}^{1+2} \rtimes O(1, 2)$, where \rtimes indicates a semidirect product. The hopping Hamiltonian $H_{\alpha} = \alpha \sum_{j=1}^3 e^{-iq_j \cdot \mathbf{r}} T_j^{\dagger} + \text{H.c.}$, breaks Lorentz invariance, continuous space translations and layer plus pseudospin rotational symmetry. The symmetry group is thus reduced to the symmorphic space-time group $\mathbb{R} \times (\mathbf{a}_1\mathbb{Z} + \mathbf{a}_2\mathbb{Z}) \rtimes D_3$, composed of time translation \mathbb{R} , discrete translations on the moiré lattice $\mathbf{a}_1\mathbb{Z} + \mathbf{a}_2\mathbb{Z}$, where \mathbf{a}_1 and \mathbf{a}_2 are the superlattice vectors, and the point group D_3 generated by the rotation C_3 around the z axis and the rotation C_2 around the x axis,

$$D_3 = \{e, C_3, C_3^2, C_2, C_2C_3, C_2C_3^2\}. \quad (\text{C1})$$

Henceforth we disregard the translational symmetries and focus on the magnetic group generated by the point group D_3 and the two special ‘‘symmetries’’ IT and P . These operations act by conjugation on the single-particle Hamiltonian H'_0 in a four-dimensional representation (4d rep.), denoted as Γ , whose unitary matrix representation we now define.

The operation C_3 rotates the bilayer by an angle $2\pi/3$ around the z axis perpendicular to the bilayer. Only the sublattice pseudospin is rotated, while the layer pseudospin is unaffected, so that

$$\Gamma(C_3) = e^{2i\pi/3\sigma_z} \tau_0. \quad (\text{C2})$$

The operation C_2 rotates the bilayer by an angle π around the x axis of Fig. 1 at mid-distance between the layers. Both sublattices and layers are flipped, so that

$$\Gamma(C_2) = \sigma_x \tau_x. \quad (\text{C3})$$

The composition of inversion I and time reversal T , denoted as IT , is antiunitary and represented by

$$\Gamma(IT) = \sigma_x \tau_0 \mathcal{K}, \quad (\text{C4})$$

where \mathcal{K} denotes the complex conjugation of the matrix elements. The operations R defined in Eqs. (C2)–(C4) are pure symmetries of the Hamiltonian, which means that $\Gamma(R)^{-1} H'_0(R\mathbf{r}, Rt) \Gamma(R) = H'_0(\mathbf{r}, t)$ for $R = C_3, C_2$, and $\Gamma(R)^{-1} H'_0(R\mathbf{r}, Rt)^* \Gamma(R) = H'_0(\mathbf{r}, t)$ for the antiunitary element $R = IT$. Finally, the unitary particle-hole operation P reverses the energy, and acts in real space as a reflection $x \mapsto -x$. Its matrix representation reads

$$\Gamma(P) = \sigma_x \tau_z. \quad (\text{C5})$$

Following Ref. [33] we define P as a unitary operation in order to have a single antiunitary generator (IT), unlike the convention of Ref. [57]. This operation is an antisymmetry of

TABLE III. Classes of conjugation of the unitary group \tilde{D}_3 , with their names (first line) and their elements (second line). e is the identity operator, \bar{e} the 2π rotation of a spin one half, and \bar{R} denotes the product $\bar{e}R$ for any operator R .

Class	e	\bar{e}	$2C_3$	$2\bar{C}_3$	$2PC_2$	$2PC_2C_3$	$2PC_2C_3^2$
Elements	$\{e\}$	$\{\bar{e}\}$	$\{C_3, C_3^2\}$	$\{\bar{C}_3, \bar{C}_3^2\}$	$\{PC_2, \bar{P}C_2\}$	$\{PC_2C_3, \bar{P}C_2C_3\}$	$\{\bar{P}C_2C_3, PC_2C_3^2\}$
Class	$6P$				$6C_2$		
Elements	$\{P, PC_3, PC_3^2, \bar{P}, \bar{P}C_3, \bar{P}C_3^2\}$			$\{C_2, C_2C_3, C_2C_3^2, \bar{C}_2, \bar{C}_2C_3, \bar{C}_2C_3^2\}$			

the Hamiltonian, which means that $\Gamma(P)^{-1}H'_0(\mathbf{Pr}, \mathbf{Pr})\Gamma(P) = -H'_0(\mathbf{r}, t)$. This antisymmetry is lost when the angular dependence of the kinetic terms $\sigma_{\pm\theta/2} \cdot \mathbf{k}$ is kept, when terms quadratic in momentum are included in the single-particle Hamiltonian, or when intervalley scattering is permitted [57]. Since Γ is faithful rep., we can infer the multiplication table of the magnetic group from that of the matrix representation of the four generators.

2. Unitary group

The unitary group \tilde{D}_3 generated by D_3 and P can be cast into the semidirect product

$$\tilde{D}_3 = \{e, P, \bar{e}, \bar{P}\} \times D_3, \tag{C6}$$

where $\bar{e} = (PC_2)^2$ and a barred operator represents the product of this operator by \bar{e} . The classes of conjugation of \tilde{D}_3 are given in Table III. The double group $D_3^D = D_3 \times \{e, \bar{e}\}$ is a normal subgroup of \tilde{D}_3 , while D_3 is not. To find the irreducible representations (irrep.) of \tilde{D}_3 —listed in Table IV—we can either find them from scratch using the composite operator method [34], or construct them by induction and other tricks from that of D_3 . Let us illustrate the second method.

The two 1d irrep. of the quotient group $\tilde{D}_3/D_3^D = \{e, P\}$ generate the irreps A_1 and a_1 . The irrep. A_1 and A_2 of D_3 induce the reps $A_1 \uparrow \tilde{D}_3 \sim A_1 \oplus a_1 \oplus E_3$ and $A_2 \uparrow \tilde{D}_3 \sim A_2 \oplus a_2 \oplus E_3$ respectively, where \oplus denotes a direct sum and \sim the equivalence of rep. The commutator subgroup $[\tilde{D}_3, \tilde{D}_3]$ is isomorphic to D_3 , whose index $|\tilde{D}_3/D_3| = 4$ gives the number of 1d irrep. Hence we have found all 1d irrep. The cardinal of the group being $|\tilde{D}_3| = 24$, the remaining irrep. are five 2d irrep., including E_3 . We can decompose the 4d rep. Γ defined by Eqs. (C2)–(C4) and (C5) as $\Gamma \sim E_1 \oplus E_5$. The 2d irrep. E of D_3 induces the rep. $E \uparrow \tilde{D}_3 \sim E_1 \oplus E_2 \oplus E_4 \oplus E_5$, where

the remaining irrep. E_2 and E_4 can be found by orthonormality of the characters.

3. Magnetic group

The group generated by \tilde{D}_3 and IT is the dichromatic magnetic group

$$\mathcal{M} = \tilde{D}_3 \times \{e, IT\}. \tag{C7}$$

To find the corepresentations (corep.) of \mathcal{M} , we apply the Schur-Frobenius criterion [35–39] to each irrep. of \tilde{D}_3 . The Schur-Frobenius criterion states the following. For any irrep ρ of \tilde{D}_3 , let us define the rep. $\rho' : \tilde{D}_3 \rightarrow M_n(\mathbb{C}), R \mapsto \rho(IT \cdot R \cdot IT^{-1})^*$. We are necessarily in one of the three following scenarios. (i) and (ii) Either ρ is equivalent to its primed counterpart, in which case there exists an invertible matrix U such that $\rho' = U\rho U^{-1}$. (i) if $UU^* = \rho(IT^2)$, there is no Kramer degeneracy: the corep. issued from ρ has the same dimension as ρ and satisfies $\rho(IT) = \pm U$. (ii) If $UU^* = -\rho(IT^2)$, the corep. issued from ρ has twice the dimension. (iii) Or ρ is not equivalent to its primed counterpart, in which case ρ' is necessarily equivalent to another irrep. of \tilde{D}_3 , and the corep. has again twice the dimension of ρ , and coincides with $\rho \oplus \rho'$ on \tilde{D}_3 .

It turns out that all irrep. of \tilde{D}_3 pertain to case (i), except E_1 and $E_5 = E'_1$, which fall into case (iii). In the former case, each irrep. leads to two corep., with $\rho(IT) = \pm 1$ for the 1d irrep. or $\rho(IT) = \pm\sigma_x$ for the 2d irrep., where σ_x represents here a generic Pauli matrix, but has nothing to do with the pseudospin. In the latter case, the one corep. formed by E_1 and E_5 is equivalent to the 4d rep. Γ . In the following, we write each corep. with an exponent \pm to indicate whether the eigenvalues of $\rho(IT)$ are $+1$ or -1 .

TABLE IV. Table of characters of the unitary group \tilde{D}_3 . Each column corresponds to a class of conjugation, and each line to an irrep. We use the symbols A and E prescribed by Mulliken’s notation; the symbol a denotes a 1d irrep. whose character differs than one on antisymmetric operators.

Irrep.	e	\bar{e}	$2C_3$	$2\bar{C}_3$	$2PC_2$	$2PC_2C_3$	$2PC_2C_3^2$	$6P$	$6C_2$
A_1	1	1	1	1	1	1	1	1	1
A_2	1	1	1	1	-1	-1	-1	1	-1
a_1	1	1	1	1	-1	-1	-1	-1	1
a_2	1	1	1	1	1	1	1	-1	-1
E_1	2	-2	-1	1	0	$\sqrt{3}$	$-\sqrt{3}$	0	0
E_2	2	2	-1	-1	2	-1	-1	0	0
E_3	2	-2	2	-2	0	0	0	0	0
E_4	2	2	-1	-1	-2	1	1	0	0
E_5	2	-2	-1	1	0	$-\sqrt{3}$	$\sqrt{3}$	0	0

TABLE V. List of the functions $f_{il}(\alpha, \beta)$ appearing in the RG flows of the four nontrivial channels a_2^-, a_1^-, E_2^+ , and E_4^- . The interaction matrices associated to each of these channels are indicated in the first line of the table.

f_{il}	$a_2^-(\sigma_z \tau_0)$	$a_1^-(\sigma_z \tau_z)$	$E_2^+(\sigma \tau_0 / \sqrt{2})$	$E_4^-(\sigma \tau_z / \sqrt{2})$
a_2^-	$\frac{4}{\pi}[1 - 12\alpha^2(1 - \beta^2)]$	$-\frac{4}{\pi}[1 - 6\alpha^2(1 - \beta^2)]$	$\frac{4}{\pi}[1 - 6\alpha^2(1 + \beta^2)]$	$\frac{4}{\pi}[1 + 6\alpha^2(3 - \beta^2)]$
a_1^-	$-\frac{4}{\pi}[1 - 6\alpha^2(1 - \beta^2)]$	$\frac{4}{\pi}$	$\frac{4}{\pi}[1 - 6\alpha^2(1 - \beta^2)]$	$\frac{4}{\pi}[1 - 6\alpha^2(1 - \beta^2)]$
E_2^+	$\frac{2}{\pi}[1 - 6\alpha^2(1 + \beta^2)]$	$\frac{2}{\pi}[1 - 6\alpha^2(1 - \beta^2)]$	$\frac{2}{\pi}[1 - 3\alpha^2(1 - \beta^2)]$	$-\frac{12}{\pi}\alpha^2\beta^2$
E_4^-	$\frac{2}{\pi}[1 + 6\alpha^2(3 - \beta^2)]$	$\frac{2}{\pi}[1 - 6\alpha^2(1 - \beta^2)]$	$-\frac{12}{\pi}\alpha^2\beta^2$	$\frac{4}{\pi}[1 + 3\alpha^2(1 + \beta^2)]$

4. Quartic interactions

The direct product $\Gamma^\dagger \otimes \Gamma$ dictates how the bilinear $\psi_i^\dagger \psi_j$ with $i, j = 1, \dots, 4$, transforms under the magnetic group \mathcal{M} . The Clebsch-Gordan series reads

$$X(\Gamma^\dagger \otimes \Gamma)X^{-1} = A_1^+ \oplus a_1^+ \oplus A_2^+ \oplus a_2^+ \oplus A_1^- \oplus a_1^- \\ \times \oplus A_2^- \oplus a_2^- \oplus E_2^+ \oplus E_4^+ \oplus E_2^- \oplus E_4^-, \quad (\text{C8})$$

where the transformation matrix X contains the Clebsch-Gordan coefficients, which can be found using the formula [35]

$$X_{ik, \gamma m} X_{jl, \gamma n}^* = \frac{n_\gamma}{|\mathcal{M}|} \sum_{R \in \mathcal{M}} \rho_\gamma(R)_{mn}^* \Gamma^\dagger(R)_{ij} \Gamma(R)_{kl}, \quad (\text{C9})$$

where ρ_γ is the γ th irrep. in the series (C8), with dimension n_γ , and $|\mathcal{M}| = 48$ is the cardinal of the magnetic group. The coefficients of the matrices \mathbf{M}_γ of Eq. (5) that transforms by conjugation according to the irrep. ρ_γ are listed in the γ th column of X , i.e., for $a, b = 1, \dots, 4$, the two components of the vector \mathbf{M}_γ read

$$(M_\gamma^{(1)})_{ab} = X_{ab, \gamma 1}, \quad (M_\gamma^{(2)})_{ab} = X_{ab, \gamma 2}. \quad (\text{C10})$$

To find the quartic interaction that preserve the magnetic group \mathcal{M} we must find all copies of the trivial irrep. A_1^+ into the product $(\Gamma^\dagger \otimes \Gamma) \otimes (\Gamma^\dagger \otimes \Gamma)$. By inspecting the characters, it is clear that only products of the same irrep. decompose themselves into a copy of A_1^+ . For the 1d irrep. $\rho = A_1^+, a_1^+, A_2^+, a_2^+, A_1^-, a_1^-, A_2^-$ and a_2^- , the decomposition is simply

$$\rho \otimes \rho = A_1^+. \quad (\text{C11})$$

Thus the quartic interaction corresponding to one of these irreps is of the form $M \otimes M$, where M is found applying Eqs. (C8) and (C10). The interaction matrices for these eight 1d irreps are listed in Table I. For the 2d irreps, we have

$$E_2^\eta \otimes E_2^\eta \sim A_1^\eta \oplus A_2^\eta \oplus E_4^\eta, \quad (\text{C12})$$

$$E_4^\eta \otimes E_4^\eta \sim A_1^\eta \oplus A_2^\eta \oplus E_2^\eta, \quad (\text{C13})$$

for $\eta = \pm$. For each of these irreps, the invariant combination transforming as A_1^+ is $M \otimes N$, where (M, N) is the basis of the two-dimensional space on which the irrep acts. The interaction matrices for these four 2d irreps are listed in Table I.

APPENDIX D: MEAN-FIELD THEORY

Here we consider only the four relevant instabilities related to interactions proportional to $\sigma_z \tau_{0/z}$ and $\sigma \tau_{0/z}$ with coupling constants $g_{0/z}$ and $\lambda_{0/z}$ respectively. The corresponding order parameters, which we denote $\Delta_{0/z}$ and $\mathcal{G}_{0/z}$, can be found in the mean-field approximation by solving the appropriate self-consistent equations. For the sake of simplicity we write down these equations separately for each instability. Upon introducing an ultraviolet cut-off Λ , these equations read

$$\Delta_{0/z} = -2g_{0/z} \int d\omega \int_\Lambda \frac{d^2 q}{(2\pi)^3} \langle \psi_{q,\omega}^\dagger \sigma_z \tau_{0/z} \psi_{q,\omega} \rangle, \quad (\text{D1a})$$

$$\mathcal{G}_{0/z} = -2\lambda_{0/z} \int d\omega \int_\Lambda \frac{d^2 q}{(2\pi)^3} \langle \psi_{q,\omega}^\dagger \sigma \tau_{0/z} \psi_{q,\omega} \rangle, \quad (\text{D1b})$$

where the momentum integral runs over a square of side Λ . The correlators in Eq. (D1) are the translationally-invariant parts of statistical averages computed over the Bloch Hamiltonian density $H'_{\text{MF}} = H'_0 + \sigma \cdot (\mathcal{G}_0 \tau_0 + \mathcal{G}_z \tau_z) + \sigma_z (\Delta_0 \tau_0 + \Delta_z \tau_z)$. The perturbative expansion of the correlators in α can be done along the lines of computing the self-energy. We have previously found that the propagator corrected by interlayer hoppings G'_0 is of the form (B11); similarly, the mean-field Hamiltonian becomes

$$H'_{\text{MF}} \mapsto N_\psi [v\sigma \cdot ((\mathbf{k} + N_0^{(G)} \mathcal{G}_0) \tau_0 + N_z^{(G)} \mathcal{G}_z \tau_z) \\ + \sigma_z (N_0^{(\Delta)} \Delta_0 \tau_0 + N_z^{(\Delta)} \Delta_z \tau_z)]. \quad (\text{D2})$$

The effect of interlayer hoppings is to enhance the order parameters by factors $N_{0/z}^{(G/\Delta)}(\alpha, \beta)$, which are the counterparts of the renormalized Fermi velocity for the matrix structures corresponding to those order parameters. They are calculated diagrammatically to sixth order in α and satisfy

$$N_\psi N_0^{(\Delta)} = 1 + 3\alpha^2(1 - \beta^2) + 2\alpha^4(1 - \beta^2)(1 + 2\beta^2) + \frac{1}{28}\alpha^6(24 - 80\beta^2 + 352\beta^4 - 233\beta^6), \quad (\text{D3a})$$

$$N_\psi N_z^{(\Delta)} = 1 - 3\alpha^2(1 - \beta^2) + 2\alpha^4(1 - \beta^2)(1 - 4\beta^2) - \frac{1}{28}\alpha^6(56 - 304\beta^2 + 872\beta^4 - 561\beta^6), \quad (\text{D3b})$$

$$vN_\psi N_0^{(G)} = 1 - 3\alpha^2 + \alpha^4(1 - \beta^2)^2 - \frac{3}{49}\alpha^6(37 - 112\beta^2 + 119\beta^4 - 70\beta^6), \quad (\text{D3c})$$

$$vN_\psi N_z^{(G)} = 1 + 3\alpha^2 + \alpha^4(1 + 10\beta^2 + \beta^4) + \frac{3}{49}\alpha^6(9 + 441\beta^4 + 70\beta^6), \quad (\text{D3d})$$

where the wavefunction normalization N_ψ is given in Appendix B. In the main text, we plotted the order parameters corrected by interlayer hoppings, i.e., the quantities $\Delta'_{0/z} = N_{0/z}^{(\Delta)} \Delta_{0/z}$ and $\mathcal{G}'_{0/z} = N_{0/z}^{(\mathcal{G})} \mathcal{G}_{0/z}$, which satisfy the self-consistency equations

$$\Delta'_{0/z} = \frac{g_{0/z} N_{0/z}^{(\Delta)} \Lambda^2}{v N_\psi} F(\Delta'_{0/z}), \quad (\text{D4a})$$

$$\mathcal{G}'_{0/z} = \frac{\lambda_{0/z} N_{0/z}^{(\Delta)} \Lambda^2}{N_\psi} F_{0/z}(\mathcal{G}'_{0/z}), \quad (\text{D4b})$$

where for simplicity we assume the shift momenta to be aligned along a crystallographic axis of the moire pattern, here along the y axis. The dimensionless functions F and $F_{0/z}$ read

$$F(x) = \frac{2x}{\pi^2} [-\log(\sqrt{x^2+2}-1) + \log(\sqrt{x^2+2}+1) - 2x \cot^{-1}(x\sqrt{x^2+2}) + 2 \coth^{-1}(\sqrt{x^2+2})], \quad (\text{D5a})$$

$$F_0(x) = \frac{1}{\pi^2} [-\sqrt{y_-} + \sqrt{y_+} + \tanh^{-1}(\sqrt{y_-}) - \tanh^{-1}(\sqrt{y_+}) - y_- \coth^{-1}(\sqrt{y_-}) + y_+ \coth^{-1}(\sqrt{y_+})], \quad (\text{D5b})$$

$$F_z(x) = \frac{1}{2\pi^2} \left[x^2 \log\left(\frac{1-x}{1+x}\right) - 2x^2 \tanh^{-1}(x) + (1-2x) \log(\sqrt{y_-}-1) - (1+2x) \log(\sqrt{y_+}-1) \right. \\ \left. + z_+ \log(\sqrt{y_+}+1) - z_- \log(\sqrt{y_-}+1) + 2(\sqrt{y_+} - \sqrt{y_-}) \right], \quad (\text{D5c})$$

where $y_\pm = 2 + x(x \pm 2)$ and $z_\pm = 1 + 2x(x \pm 1)$.

APPENDIX E: RENORMALIZATION

1. Hubbard-Stratonovitch decoupling

We aim at finding the most relevant insulating state near charge neutrality. It is therefore practical to decouple the interactions in the direct, particle-hole channel, to evince order parameters of the form $\langle \psi^\dagger M \psi \rangle$ for $M \in \{R_i, \mathbf{M}_j\}$, where the bracket $\langle \dots \rangle$ denotes the ensemble average over the complete action $S = S'_0 + S_{\text{int}}$.

Using Hubbard-Stratonovitch transformations, we introduce one auxiliary bosonic field for each interaction, whose ground-state value in the correlated phase is a constant solution of the classical equation of motion. We must distinguish between the 1d corep., for which a scalar field ϕ_i for $i = 1, \dots, 8$, is sufficient, and the 2d corep., for which a two-component field $\boldsymbol{\varphi}_j = \{\varphi_{j,1}, \varphi_{j,2}\}$ must be introduced, for $j = 9, \dots, 12$. Such transformation enables to recast the action for quartic fermion interactions (5) into

$$S_{\text{int}}[\psi^\dagger, \psi] \rightarrow S_{\text{Hub}}[\psi^\dagger, \psi, \phi] \\ = \sum_{i=1}^8 \int d^2r d\tau (\phi_i^2 + 2\sqrt{g_i} \psi^\dagger \phi_i R_i \psi) \\ + \sum_{j=9}^{12} \int d^2r d\tau (\boldsymbol{\varphi}_j^2 + 2\sqrt{\lambda_j} \psi^\dagger \boldsymbol{\varphi}_j \cdot \mathbf{M}_j \psi), \quad (\text{E1})$$

where the sum runs over both 1d and 2d irreps.. For simplicity we dropped the spatial and time dependencies of the fields in Eq. (E1). The action for quartic fermion interactions thus splits into a bosonic quadratic action (the first term in the parenthesis), and a three-point vertex, which takes the form of a Yukawa coupling (the second term in the parenthesis).

2. Renormalization procedure

The field theory described by the sum of action S'_0 and action S_{Hub} (E1) has critical dimension $d_c = 2$, which entails

that in $d = 3$ space-time dimensions, we expect that all interactions lead to quantum critical points that are perturbative in the small parameter $\epsilon = d - 2$. From now onwards, we work in Fourier space and express all fields and integrals in terms of the momentum \mathbf{q} and the Matsubara frequency ω . A general Fourier-transformed field is written $\phi_{\mathbf{q},\omega}$ for the bosonic case, or $\{\psi_{\mathbf{q},\omega}, \psi_{\mathbf{q},\omega}^\dagger\}$ for the fermionic case, where $\psi_{\mathbf{q},\omega}^\dagger = (\psi_{\mathbf{q},\omega})^\dagger$ denotes the conjugate of the Fourier-transformed field $\psi_{\mathbf{q},\omega}$. To renormalize the field theory, we assume that the complete action S is actually expressed in terms of bare fields $\{\phi, \psi\}$ for $\phi \in \{\phi_i, \boldsymbol{\varphi}_j\}$ and couplings \hat{g} for $g \in \{g_i, \lambda_j\}$, which are ill defined in the interacting theory. The physical parameters and fields—written without the \circ symbol—are connected to their bare counterparts through the so-called Z constants.

We define the Z constants for the fields such that

$$\hat{\phi} = Z_\phi^{1/2} \phi, \quad \hat{\psi} = Z_\psi^{1/2} \psi. \quad (\text{E2})$$

To regularize the theory, we work in an isotropic space-time of dimension $d = 2 + \epsilon$, and introduce a mass scale μ to make the regularized couplings dimensionless. A renormalized coupling g is linked to its bare value \hat{g} by

$$\hat{g} = \mu^{-\epsilon} N_\psi^2 Z_g^2 Z_\phi^{-1} g. \quad (\text{E3})$$

We included the normalization of the wavefunction N_ψ in the redefinition of the couplings in order to compensate at all loop orders those arising from the corrected fermionic propagator G'_0 , given in Eq. (B11). Owing to dimensional regularization, we must promote the Pauli matrices in S_0 to a Clifford algebra in arbitrary dimension d , satisfying the anticommutation rules $\{\sigma_i, \sigma_j\} = 2\delta_{ij}$ for $i, j = 1, \dots, d$. Using Eqs. (E2) and (E3), we find the renormalized action $S_{\text{R}} = S_{\text{R},0} + S_{\text{R},\alpha} + S_{\text{R},\phi} + S_{\text{R,int}}$, where the quadratic, decoupled action reads

$$S_{\text{R},0} = \int_{\mathbf{q},\omega} \psi_{\mathbf{q}}^\dagger (\boldsymbol{\sigma} \cdot \mathbf{q} \tau_0 - i\omega \sigma_0 \tau_0) \psi_{\mathbf{q}}. \quad (\text{E4})$$

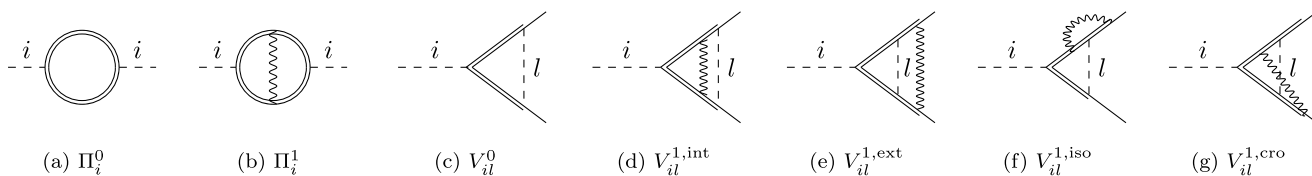


FIG. 9. One-particle irreducible diagrams at one loop, up to order two in interlayer hoppings. The double line stands for the fermionic propagator corrected by interlayer hoppings of Fig. 8(f), the dashed line for the bosonic propagator, and the wavy line for the sum of interlayer hoppings of opposite momenta $\pm\eta\mathbf{q}_j$, for $\eta = \pm$ and $j = 1, 2, 3$. Polarization Π_i at zero external momentum and fixed Matsubara frequency, for the field ϕ_i at order (a) α^0 and (b) α^2 . Three-point vertex V_{il} at order (c) α^0 and [(d)–(g)] α^2 , whose hopping line is (d) internal, (e) external, (f) isolated, and (g) crossed.

The quadratic hopping action reads

$$S_{R,\alpha} = \alpha \sum_{\eta} \sum_{j=1}^3 \int_{q,\omega} \psi_q^\dagger T_j^\eta \psi_{q+\eta\mathbf{q}_j}. \quad (\text{E5})$$

The renormalized bosonic part of the action is given by

$$S_{R,\phi} = \sum_{i=1}^8 Z_{\phi_i} \int_{q,\omega} (\phi_i^2)_q + \sum_{j=8}^{12} Z_{\varphi_j} \int_{q,\omega} (\varphi_j^2)_q. \quad (\text{E6})$$

Finally, the renormalized interaction between fermionic and bosonic fields is

$$S_{R,\text{int}} = 2\mu^{-\epsilon/2} N_\psi \left[\sum_{i=1}^8 Z_{g_i} \sqrt{g_i} \int_{q,\omega_q,p,\omega_p} \psi_q^\dagger (\phi_i)_{q-p} R_i \psi_p + \sum_{j=1}^{12} Z_{\lambda_j} \sqrt{\lambda_j} \int_{q,\omega_q,p,\omega_p} \psi_q^\dagger (\varphi_j)_{q-p} \mathbf{M}_j \psi_p \right]. \quad (\text{E7})$$

In Eqs. (E4)–(E7), we have omitted dependence of the fields on frequency and used the shorthand

$$\int_{q,\omega} = \int_{\mathbb{R}^d} \frac{d^{d-1}q d\omega}{(2\pi)^d}. \quad (\text{E8})$$

To fix values of the Z constants we use the minimal subtraction (MS) scheme, i.e., we absorb in them only the divergent parts of the diagrams. Inspecting Eqs. (E6) and (E7), we see that the constant Z_ϕ can be found from the divergences of the polarization, i.e. the bosonic self-energy, while the constant Z_g can be determined by absorbing the divergences of the three-point vertices. Before computing explicitly the diagrams for the polarization and vertices let us outline the general strategy.

3. Preliminary mathematical remarks

Taking into account the interlayer hopping is done into two steps. We first draw the diagrams without insertion the hopping matrices, and then replace all solid lines by double lines. This corresponds to replacing free propagators by the propagators dressed by interlayer hoppings, like in the polarization shown in Fig. 9(a). In second step we include wavy lines, i.e., hopping matrices, connecting different propagators [see Fig. 9(b)]. This splitting allows us to explicitly extract factors of v^{-1} , where v is the Fermi velocity corrected by interlayer hoppings (B12) and which vanishes at the first magic

angle. We restrict our computation to order α^2 , which is the first nontrivial order.

When expanding product of matrices and integrating the trace, useful relations can be found in Refs. [59–61]. The Feynman trick,

$$\frac{1}{AB} = \int_0^1 \frac{dx}{Ax + B(1-x)}, \quad (\text{E9})$$

valid for any expressions A and B , enable to linearize products of denominators. For the four relevant interactions we consider here, the space-time integrals are isotropic and can be computed in arbitrary dimension d using

$$\int \frac{d^d Q}{(2\pi)^d} \frac{Q^{2a}}{(Q^2 + m^2)^b} = \frac{\Gamma(b-a-d/2)\Gamma(a+d/2)}{(4\pi)^{d/2}\Gamma(b)\Gamma(d/2)} m^{-2(b-a-d/2)}, \quad (\text{E10})$$

for any reals a and b , and where $Q = (\mathbf{q}, \omega)$ is the relativistic d momentum. The dummy mass $m \rightarrow 0$ plays the role of an infrared regulator and Γ denotes Euler's Gamma function, which satisfies

$$\Gamma(-n+x) = \frac{(-1)^n}{n!} \left[\frac{1}{x} + \Psi(n+1) + \mathcal{O}(x) \right] \quad (\text{E11})$$

for all real x and integer n ; this relation is usually used with $x = \epsilon$. In Eq. (E11), $\Psi = (\ln \Gamma)$ is Euler's Digamma function, which does not intervene at one loop, since we discard all finite quantities in the MS scheme.

4. Polarization

The one-loop polarization Π_i is the self-energy of the auxiliary field ϕ_i (for $i = 1, \dots, 12$). If $\Delta_i(\mathbf{k}, \Omega)$ denotes the corrected propagator of the bosonic field, we have $\Delta_i^{-1}(\mathbf{k}, \Omega) = Z_\phi - \Pi_i(\mathbf{k}, \Omega)$. The one-loop diagrams contributing to the polarization at zero external momentum $\mathbf{k} = \mathbf{0}$ and fixed frequency Ω are drawn in Fig. 9. The polarization at order α^0 reads

$$\Pi_i^0 = -4g_i N_\psi^2 \int_{q,\omega} \text{Tr}[\mathbf{M}_i G'_0(\mathbf{q}, \omega) \cdot \mathbf{M}_i G'_0(\mathbf{q}, \omega)]. \quad (\text{E12})$$

Notice that for the sake of generality, we will write all interaction matrices as the vectors \mathbf{M}_i , which can either denote a single matrix R_i for $i = 1, \dots, 8$, or a two-component vector

\mathbf{M}_i for $i = 8, \dots, 12$. The polarization at order α^2 reads

$$\begin{aligned} \Pi_i^1 = & -4g_i N_\psi^2 \alpha^2 \sum_{\eta,j} \int_{\mathbf{q},\omega} \text{Tr}[\mathbf{M}_i G'_0(\mathbf{q}, \omega) T_j^{\bar{\eta}} G'_0(\mathbf{q} + \eta \mathbf{q}_j, \omega) \\ & \cdot \mathbf{M}_i G'_0(\mathbf{q} + \eta \mathbf{q}_j, \omega) T_j^\eta G'_0(\mathbf{q}, \omega)]. \end{aligned} \quad (\text{E13})$$

The pole of the integral in Eq. (E12) per number of fermion flavors n (equal to four in our case), is given by $\Pi_i^0 = -4ng_i I_i / v\epsilon$ where

$$\begin{aligned} I_i = & \lim_{\epsilon \rightarrow 0} \frac{v\epsilon N_\psi^2}{n} \int_{\mathbf{q},\omega} \text{Tr}[\mathbf{M}_i G'_0(\mathbf{q}, \omega) \cdot \mathbf{M}_i G'_0(\mathbf{q}, \omega)] \\ = & \begin{cases} \frac{1}{2\pi} & \text{if } \mathbf{M}_i \text{ has the sublattice structure } \sigma_z, \\ \frac{1}{4\pi} & - \sigma. \end{cases} \end{aligned} \quad (\text{E14})$$

In Eq. (E13) we can use again the separation of energy scales: The theory is meaningful only at low energy, i.e., for $\mathbf{q}, \omega \ll 1$, so that $G'_0(\mathbf{q} + \eta \mathbf{q}_j, \omega)$ can be replaced by

$$V_{il}^0 = N_\psi^3 (2\sqrt{g_i})(4g_l) \int_{\mathbf{q},\omega} \mathbf{M}_l G'_0(\mathbf{q}, \omega) \mathbf{M}_i G'_0(\mathbf{q}, \omega) \cdot \mathbf{M}_l. \quad (\text{E16})$$

The three-point vertex at order α^2 (mixed diagram with two interlayer hopping) have either multiplicity one, or two. Those with multiplicity one nest either an internal hopping line, as in Fig. 9(d),

$$V_{il}^{1,\text{int}} = N_\psi^3 (2\sqrt{g_i})(4g_l \alpha^2) \sum_{\eta,j} \int_{\mathbf{q},\omega} \mathbf{M}_l G'_0(\mathbf{q}, \omega) T_j^{\bar{\eta}} G'_0(\mathbf{q} + \eta \mathbf{q}_j, \omega) \mathbf{M}_i G'_0(\mathbf{q} + \eta \mathbf{q}_j, \omega) T_j^\eta G'_0(\mathbf{q}, \omega) \cdot \mathbf{M}_l, \quad (\text{E17})$$

or an external hopping line, as in Fig. 9(e),

$$V_{il}^{1,\text{ext}} = N_\psi^3 (2\sqrt{g_i})(4g_l \alpha^2) \sum_{\eta,j} \int_{\mathbf{q},\omega} T_j^{\bar{\eta}} G'_0(\eta \mathbf{q}_j, \omega) \mathbf{M}_l G'_0(\mathbf{q}, \omega) \mathbf{M}_i G'_0(\mathbf{q}, \omega) \cdot \mathbf{M}_l G'_0(\eta \mathbf{q}_j, \omega) T_j^\eta. \quad (\text{E18})$$

The mixed diagrams with multiplicity two nest either an isolated hopping line, as in Fig. 9(f),

$$V_{il}^{1,\text{iso}} = 2N_\psi^3 (2\sqrt{g_i})(4g_l \alpha^2) \sum_{\eta,j} \int_{\mathbf{q},\omega} T_j^{\bar{\eta}} G'_0(\eta \mathbf{q}_j, \omega) \mathbf{M}_l G'_0(\mathbf{q} + \eta \mathbf{q}_j, \omega) T_j^\eta G'_0(\mathbf{q}, \omega) \mathbf{M}_i G'_0(\mathbf{q}, \omega) \cdot \mathbf{M}_l, \quad (\text{E19})$$

or a hopping line that crosses the interaction line, shown in Fig. 9(g),

$$V_{il}^{1,\text{cro}} = 2N_\psi^3 (2\sqrt{g_i})(4g_l \alpha^2) \sum_{\eta,j} \int_{\mathbf{q},\omega} \mathbf{M}_l G'_0(\bar{\eta} \mathbf{q}_j, \omega) T_j^{\bar{\eta}} G'_0(\mathbf{q}, \omega) \mathbf{M}_i G'_0(\mathbf{q}, \omega) \cdot \mathbf{M}_l G'_0(\eta \mathbf{q}_j, \omega) T_j^\eta. \quad (\text{E20})$$

Similarly, we can define the pole of the integral appearing in Eq. (E16) as

$$J_{il} = \lim_{\epsilon \rightarrow 0} \frac{v\epsilon N_\psi^2}{n} \int_{\mathbf{q},\omega} \text{Tr}[\mathbf{M}_l G'_0(\mathbf{q}, \omega) \mathbf{M}_i G'_0(\mathbf{q}, \omega) \cdot \mathbf{M}_l \mathbf{M}_i] = \begin{cases} 0 & \text{if } (\mathbf{M}_i, \mathbf{M}_l) \text{ match } (\sigma, \sigma), \\ \frac{-1}{4\pi} & - (\sigma, \sigma_z), \\ \frac{-1}{2\pi} & - (\sigma_z, \sigma), \\ \frac{1}{2\pi} & - (\sigma_z, \sigma_z), \end{cases} \quad (\text{E21})$$

such that $V_{il}^{1,\text{in}} = V_{il}^{1,\text{ext}} = 3\alpha^2 \chi_i h_i(\beta) V_{il}^0$ with $V_{il}^0 = N_\psi (2i\sqrt{g_i})(4g_l J_{il} / v\epsilon)$. We also define the pole appearing in the sum of the diagrams with multiplicity two as

$$K_{il}(\beta) = \lim_{\epsilon \rightarrow 0} \frac{v\epsilon N_\psi^4}{n} \sum_{\eta,j} \int_{\mathbf{q},\omega} \text{Tr}[\mathbf{M}_l G'_0(\eta \mathbf{q}_j, \omega) T_j^\eta G'_0(\mathbf{q}, \omega) \mathbf{M}_i G'_0(\mathbf{q}, \omega) \cdot \mathbf{M}_l (\mathbf{M}_i T_j^{\bar{\eta}} G'_0(\eta \mathbf{q}_j, \omega) + G'_0(\bar{\eta} \mathbf{q}_j, \omega) T_j^{\bar{\eta}} \mathbf{M}_i)], \quad (\text{E22})$$

such that $V_{il}^{1,\text{iso}} + V_{il}^{1,\text{cro}} = N_\psi (2i\sqrt{g_i})(8\alpha^2 g_l K_{il}(\beta) / v\epsilon)$. The integrals J_{il} are numerical constants, dependent of neither the number of fermion flavors n nor the corrugation parameter β , while $K_{il}(\beta)$ depends on the corrugation parameter. Using

$G'_0(\eta \mathbf{q}_j, 0)$. This results in $\Pi_i^1 = -3\alpha^2 \chi_i h_i(\beta) \Pi_i^0$ where χ_i equals either +1 for the interaction matrices $\sigma_z \tau_0$ and $\sigma \tau_z$ or -1 for the interaction matrices $\sigma_z \tau_z$ and $\sigma \tau_0$; and the corrugation-dependent function $h_i(\beta)$ equals either $1 - \beta^2$ or 1 if the interaction matrix matches σ_0 or σ_z in the pseudospin sector, respectively. This fixes the renormalization constant to

$$Z_{\phi_i} = 1 - \frac{4ng_i I_i [1 + 3\alpha^2 \chi_i h_i(\beta)]}{v\epsilon}. \quad (\text{E15})$$

5. Vertices

We denote the one-loop contribution to the three-point vertex of interaction i renormalized by interaction l by V_{il} . The one-loop vertices at zero external momentum $\mathbf{k} = \mathbf{0}$ and fixed frequency Ω are drawn in Figs. 9(c)–9(g) and computed in Eqs. (E16)–(E20). For the vertices correcting an interaction i associated to a 2d channel, we write the vertex for only one component of the matrix \mathbf{M}_i , simply denoted as M_i . The three-point vertex at order α^0 , given by diagram shown in Fig. 9(c), reads

commutation relations between interaction and hopping matrices, we can express all vertices (E16)–(E20) in terms of J_{il} and K_{il} only. We then find the vertex renormalization constant to be

$$Z_{g_i} = 1 - \frac{4}{v\epsilon} \sum_l g_l [(1 + 6\alpha^2 h_i(\beta)\chi_i)J_{il} + 2\alpha^2 K_{il}(\beta)]. \quad (\text{E23})$$

6. RG flow equations

We express $Z_i = Z_{g_i}^2 Z_{\phi_i}^{-1}$ to first order in the coupling constants as

$$Z_i = 1 + \sum_{l=1}^{12} \frac{f_{il}(\alpha, \beta)g_l}{v\epsilon}, \quad (\text{E24})$$

where

$$f_{il}(\alpha, \beta) = 4[(nI_i\delta_{il} - 2J_{il}) + 3\alpha^2 h_i(\beta)\chi_i(nI_i\delta_{il} - 4J_{il}) - 4\alpha^2 K_{il}(\beta)]. \quad (\text{E25})$$

and v is the Fermi velocity (B12). We provide the explicit expressions of the f_{il} functions in terms of α, β for the four non-trivial channels $a_2^-, a^-1, E_2^+, E_4^-$ in Table V. We compute the RG flow equations by deriving Eq. (E3) with respect to μ at constant bare couplings. This yields

$$-\frac{\partial \log g_i}{\partial \log \mu} = -\epsilon + v^{-1} \sum_{l=1}^{12} f_{il}(\alpha, \beta)g_l. \quad (\text{E26})$$

-
- [1] R. B. Laughlin, Anomalous Quantum Hall Effect: An Incompressible Quantum Fluid with Fractionally Charged Excitations, *Phys. Rev. Lett.* **50**, 1395 (1983).
- [2] N. Nagaosa, J. Sinova, S. Onoda, A. H. MacDonald, and N. P. Ong, Anomalous Hall effect, *Rev. Mod. Phys.* **82**, 1539 (2010).
- [3] R. Bistritzer and A. H. MacDonald, Moire bands in twisted double-layer graphene, *Proc. Natl. Acad. Sci. USA* **108**, 12233 (2011).
- [4] S. Shallcross, S. Sharma, E. Kandelaki, and O. A. Pankratov, Electronic structure of turbostratic graphene, *Phys. Rev. B* **81**, 165105 (2010).
- [5] R. Bistritzer and A. H. MacDonald, Moiré butterflies in twisted bilayer graphene, *Phys. Rev. B* **84**, 035440 (2011).
- [6] G. Tarnopolsky, A. J. Kruchkov, and A. Vishwanath, Origin of Magic Angles in Twisted Bilayer Graphene, *Phys. Rev. Lett.* **122**, 106405 (2019).
- [7] Y. Cao, V. Fatemi, A. Demir, S. Fang, S. L. Tomarken, J. Y. Luo, J. D. Sanchez-Yamagishi, K. Watanabe, T. Taniguchi, E. Kaxiras *et al.*, Correlated insulator behaviour at half-filling in magic-angle graphene superlattices, *Nature (London)* **556**, 80 (2018).
- [8] Y. Cao, V. Fatemi, S. Fang, K. Watanabe, T. Taniguchi, E. Kaxiras, and P. Jarillo-Herrero, Unconventional superconductivity in magic-angle graphene superlattices, *Nature (London)* **556**, 43 (2018).
- [9] M. Yankowitz, S. Chen, H. Polshyn, Y. Zhang, K. Watanabe, T. Taniguchi, D. Graf, A. F. Young, and C. R. Dean, Tuning superconductivity in twisted bilayer graphene, *Science* **363**, 1059 (2019).
- [10] L. Balents, C. R. Dean, D. K. Efetov, and A. F. Young, Superconductivity and strong correlations in moiré flat bands, *Nat. Phys.* **16**, 725 (2020).
- [11] G. Chen, A. L. Sharpe, P. Gallagher, I. T. Rosen, E. J. Fox, L. Jiang, B. Lyu, H. Li, K. Watanabe, T. Taniguchi *et al.*, Signatures of tunable superconductivity in a trilayer graphene moiré superlattice, *Nature (London)* **572**, 215 (2019).
- [12] G. Chen, A. L. Sharpe, E. J. Fox, Y.-H. Zhang, S. Wang, L. Jiang, B. Lyu, H. Li, K. Watanabe, T. Taniguchi *et al.*, Tunable correlated Chern insulator and ferromagnetism in trilayer graphene/boron nitride moiré superlattice, *Nature (London)* **579**, 56 (2020).
- [13] M. Serlin, C. L. Tschirhart, H. Polshyn, Y. Zhang, J. Zhu, K. Watanabe, T. Taniguchi, L. Balents, and A. F. Young, Intrinsic quantized anomalous Hall effect in a moiré heterostructure, *Science* **367**, 900 (2020).
- [14] Y. Xie, B. Lian, B. Jäck, X. Liu, C.-L. Chiu, K. Watanabe, T. Taniguchi, B. A. Bernevig, and A. Yazdani, Spectroscopic signatures of many-body correlations in magic-angle twisted bilayer graphene, *Nature (London)* **572**, 101 (2019).
- [15] Y. W. Choi and H. J. Choi, Strong electron-phonon coupling, electron-hole asymmetry, and nonadiabaticity in magic-angle twisted bilayer graphene, *Phys. Rev. B* **98**, 241412(R) (2018).
- [16] B. Roy and V. Juricic, Unconventional superconductivity in nearly flat bands in twisted bilayer graphene, *Phys. Rev. B* **99**, 121407(R) (2019).
- [17] F. Wu, A. H. MacDonald, and I. Martin, Theory of Phonon-Mediated Superconductivity in Twisted Bilayer Graphene, *Phys. Rev. Lett.* **121**, 257001 (2018).
- [18] G. Sharma, M. Trushin, O. P. Sushkov, G. Vignale, and S. Adam, Superconductivity from collective excitations in magic angle twisted bilayer graphene, *Phys. Rev. Research* **2**, 022040 (2020).
- [19] X. Gu, C. Chen, J. N. Leaw, E. Laksono, V. M. Pereira, G. Vignale, and S. Adam, Antiferromagnetism and chiral d-

- wave superconductivity from an effective $t - J - D$ model for twisted bilayer graphene, *Phys. Rev. B* **101**, 180506 (2020).
- [20] F. Wu and S. Das Sarma, Identification of superconducting pairing symmetry in twisted bilayer graphene using in-plane magnetic field and strain, *Phys. Rev. B* **99**, 220507(R) (2019).
- [21] M. Angeli, E. Tosatti, and M. Fabrizio, Valley Jahn-Teller effect in twisted bilayer graphene, *Phys. Rev. X* **9**, 041010 (2019).
- [22] Y. Cao, D. Rodan-Legrain, J. M. Park, F. N. Yuan, K. Watanabe, T. Taniguchi, R. M. Fernandes, L. Fu, and P. Jarillo-Herrero, Nematicity and Competing Orders in Superconducting Magic-Angle Graphene, [arXiv:2004.04148](https://arxiv.org/abs/2004.04148).
- [23] X. Lu, P. Stepanov, W. Yang, M. Xie, M. A. Aamir, I. Das, C. Urgell, K. Watanabe, T. Taniguchi, G. Zhang *et al.*, Superconductors, orbital magnets and correlated states in magic-angle bilayer graphene, *Nature (London)* **574**, 653 (2019).
- [24] Y. Jiang, X. Lai, K. Watanabe, T. Taniguchi, K. Haule, J. Mao, and E. Y. Andrei, Charge order and broken rotational symmetry in magic-angle twisted bilayer graphene, *Nature (London)* **573**, 91 (2019).
- [25] A. Kerelsky, L. J. McGilly, D. M. Kennes, L. Xian, M. Yankowitz, S. Chen, K. Watanabe, T. Taniguchi, J. Hone, C. Dean *et al.*, Maximized electron interactions at the magic angle in twisted bilayer graphene, *Nature (London)* **572**, 95 (2019).
- [26] J. M. B. Lopes dos Santos, N. M. R. Peres, and A. H. Castro Neto, Graphene Bilayer with a Twist: Electronic Structure, *Phys. Rev. Lett.* **99**, 256802 (2007).
- [27] As is standard, we keep only the linear part of the dispersion relation, and neglect the $\pm\theta/2$ twists of the wavevectors near the cones and spin-orbit coupling.
- [28] A. B. Kuzmenko, I. Crassee, D. van der Marel, P. Blake, and K. S. Novoselov, Determination of the gategunable band gap and tight-binding parameters in bilayer graphene using infrared spectroscopy, *Phys. Rev. B* **80**, 165406 (2009).
- [29] M. Koshino, N. F. Q. Yuan, T. Koretsune, M. Ochi, K. Kuroki, and L. Fu, Maximally localized Wannier orbitals and the extended Hubbard model for twisted bilayer graphene, *Phys. Rev. X* **8**, 031087 (2018).
- [30] P. Lucignano, D. Alfè, V. Cataudella, D. Ninno, and G. Cantele, The crucial role of atomic corrugation on the flat bands and energy gaps of twisted bilayer graphene at the “magic angle” $\theta \sim 1.08^\circ$, *Phys. Rev. B* **99**, 195419 (2019).
- [31] Note that in Eq. (5) the interactions, which are off-diagonal in layer acquire an \mathbf{r} dependence as a consequence of our choice of coordinates for the fields in Eq. (1).
- [32] This antisymmetry is lost when the angular dependence of the kinetic terms $\sigma_{\pm\theta/2} \cdot \mathbf{k}$ is kept, when terms, which are quadratic in momentum are included in the single-particle Hamiltonian, or when intervalley scattering is permitted [57].
- [33] K. Hejazi, C. Liu, H. Shapourian, X. Chen, and L. Balents, Multiple topological transitions in twisted bilayer graphene near the first magic angle, *Phys. Rev. B* **99**, 035111 (2019).
- [34] J. Chen, J. Ping, and F. Wang, *Group Representation Theory for Physicists*, Second edition (World Scientific, Singapore, 2002).
- [35] M. Zhong-qi, *Group Theory for Physicists* (World Scientific, Singapore, 2007).
- [36] M. Zhong-qi and G. Xiao-yan, *Problems and Solutions in Group Theory for Physicists* (World Scientific, Singapore, 2004).
- [37] P. Atkins, M. Child, and C. Phillips, *Tables for group theory* (Oxford University Press, Oxford, 1970).
- [38] M. Dresselhaus, G. Dresselhaus, and A. Jorio, *Group Theory: Application to the Physics of Condensed Matter* (Springer, Berlin Heidelberg, 2007).
- [39] P. Woit, *Quantum Theory, Groups and Representations: An Introduction* (Springer International Publishing, New York, 2017).
- [40] Note that we neglected the \mathbf{r} dependence in these expressions for the sake of clarity.
- [41] The momentum integrals run over a finite square of the size the ultraviolet cut-off Λ .
- [42] E. Codecido, Q. Wang, R. Koester, S. Che, H. Tian, R. Lv, S. Tran, K. Watanabe, T. Taniguchi, F. Zhang *et al.*, Correlated insulating and superconducting states in twisted bilayer graphene below the magic angle, *Sci. Adv.* **5**, eaaw9770 (2019).
- [43] T. Giamarchi, *Quantum Physics in One Dimension* (Clarendon Press, Oxford, 2003), Vol. 121.
- [44] R. Shankar, Renormalization-group approach to interacting fermions, *Rev. Mod. Phys.* **66**, 129 (1994).
- [45] L. Classen, I. F. Herbut, L. Janssen, and M. M. Scherer, Mott multicriticality of Dirac electrons in graphene, *Phys. Rev. B* **92**, 035429 (2015).
- [46] B. Rosenstein, B. J. Warr, and S. H. Park, Dynamical symmetry breaking in four-fermion interaction models, *Phys. Rep.* **205**, 59 (1991).
- [47] As is the case for the magic angle value, the renormalization flow weakly depends on corrugation effects, i.e., on β . The major impact of corrugation is to slow down the shrinking of the semimetallic region by pushing away the crossover point from the origin as β decreases from 1.
- [48] E. Fradkin, S. A. Kivelson, M. J. Lawler, J. P. Eisenstein, and A. P. Mackenzie, Nematic fermi fluids in condensed matter physics, *Annu. Rev. Condens. Matter Phys.* **1**, 153 (2010).
- [49] Y. Choi, J. Kemmer, Y. Peng, A. Thomson, H. Arora, R. Polski, Y. Zhang, H. Ren, J. Alicea, G. Refaelt *et al.*, Electronic correlations in twisted bilayer graphene near the magic angle, *Nat. Phys.* **15**, 1174 (2019).
- [50] P. Stepanov, I. Das, X. Lu, A. Fahimniya, K. Watanabe, T. Taniguchi, F. H. Koppens, J. Lischner, L. Levitov, and D. K. Efetov, Untying the insulating and superconducting orders in magic-angle graphene, *Nature (London)* **583**, 375 (2020).
- [51] S. Liu, E. Khalaf, J. Y. Lee, and A. Vishwanath, Nematic topological semimetal and insulator in magic angle bilayer graphene at charge neutrality, *Phys. Rev. Research* **3**, 013033 (2021).
- [52] M. Ochi, M. Koshino, and K. Kuroki, Possible correlated insulating states in magic-angle twisted bilayer graphene under strongly competing interactions, *Phys. Rev. B* **98**, 081102(R) (2018).
- [53] J. Kang and O. Vafek, Strong Coupling Phases of Partially Filled Twisted Bilayer Graphene Narrow Bands, *Phys. Rev. Lett.* **122**, 246401 (2019).
- [54] N. Bultinck, E. Khalaf, S. Liu, S. Chatterjee, A. Vishwanath, and M. P. Zaletel, Ground state and hidden symmetry of magic angle graphene at even integer filling, *Phys. Rev. X* **10**, 031034 (2020).
- [55] D. V. Chichinadze, L. Classen, and A. V. Chubukov, Orbital antiferromagnetism, nematicity, and density wave orders in twisted bilayer graphene, *Phys. Rev. B* **102**, 125120 (2020).
- [56] Y. Zhang, K. Jiang, Z. Wang, and F. Zhang, Correlated insulating phases of twisted bilayer graphene at commensurate filling fractions: a hatree-fock study, *Phys. Rev. B* **102**, 035136 (2020).

- [57] Z. Song, Z. Wang, W. Shi, G. Li, C. Fang, and B. A. Bernevig, All Magic Angles in Twisted Bilayer Graphene are Topological, *Phys. Rev. Lett.* **123**, 036401 (2019).
- [58] L. Balents, General continuum model for twisted bilayer graphene and arbitrary smooth deformations, *SciPost Phys.* **7**, 048 (2019).
- [59] M. Srednicki, *Quantum Field Theory* (Cambridge University Press, Cambridge, 2007).
- [60] H. Kleinert and V. Schulte-Frohlinde, *Critical Properties of ϕ^4 -theories* (World Scientific, Singapore, 2001).
- [61] J. Zinn-Justin, *Quantum Field Theory and Critical Phenomena*, International series of monographs on physics (Clarendon Press, Oxford, 2002).